Bedform migration in a mixed sand and cohesive clay intertidal environment and implications for bed material transport predictions

Lichtman, Ian D.; Baas, Jacobus Hugo; Amoudry, Laurent O.; Thorne, Peter D.; Malarkey, Jonathan; Hope, Julie A.; Peakall, Jeffrey; Paterson, David M.; Bass, Sarah J.; Cooke, Richard D.; Manning, Andrew J.; Davies, Alan G.; Parsons, Daniel R.; Ye, Leiping

Geomorphology

DOI:
10.1016/j.geomorph.2018.04.016

Published: 15/08/2018

Peer reviewed version

Bedform migration in a mixed sand and cohesive clay intertidal environment and implications for bed material transport predictions

Ian D. Lichtman[1,2,*], Jaco H. Baas[2], Laurent O. Amoudry[1], Peter D. Thorne[1], Jonathan Malarkey[2], Julie A. Hope[3], Jeffrey Peakall[4], David M. Paterson[5], Sarah J. Bass[6], Richard D. Cooke[1], Andrew J. Manning[6,7,8], Alan G. Davies[2], Daniel R. Parsons[7], and Leiping Ye[7]

[1] National Oceanography Centre, Joseph Proudman Building, 6 Brownlow Street, Liverpool, L3 5DA, United Kingdom

[2] School of Ocean Sciences, Bangor University, Menai Bridge, Isle of Anglesey, LL59 5AB, United Kingdom

[3] Institute of Marine Science, The University of Auckland, Auckland 1142, New Zealand

[4] School of Earth and Environment, University of Leeds, LS2 9JT, United Kingdom

[5] Scottish Oceans Institute, School of Biology, University of St. Andrews, St. Andrews, KY16 8LB, United Kingdom

[6] School of Marine Science and Engineering, Plymouth University, PL4 8AA, United Kingdom

[7] Department of Geography, Environment and Earth Sciences, University of Hull, Hull, HU6 7RX, United Kingdom

[8] HR Wallingford, Howbery Park, Wallingford, OX10 8BA, United Kingdom

* Correspondence to: I. D. Lichtman, doulich@noc.ac.uk

Highlights

Transport by sand-mud bedforms with varying cohesive content is compared to pure sand bedforms

Cohesion affects bed material transport at remarkably low clay and EPS fractions of <2.8% and <0.05%

Bedload transport predictors in sand with even small amounts of clay and EPS need modification

Abstract

Many coastal and estuarine environments are dominated by mixtures of non-cohesive sand and cohesive mud. The migration rate of bedforms, such as ripples and dunes, in these environments is important in determining bed material transport rates to inform and assess numerical models of sediment transport and geomorphology. However, these models tend to ignore parameters describing the physical and biological cohesion (resulting from clay and extracellular polymeric substances, EPS) in natural mixed sediment, largely because of a scarcity of relevant laboratory and field data. To address this gap in knowledge, data were collected on intertidal flats over a spring-neap cycle to determine the bed material transport rates of bedforms in biologically-active mixed sand-mud. Bed cohesive composition changed from below 2 volume % up to 5.4 volume % cohesive clay, as the tide progressed from spring towards neap. The amount of EPS in the bed sediment was found to vary linearly with the clay content. Using multiple linear regression, the transport rate was found to depend on the Shields stress parameter and the bed cohesive clay content. The transport rates decreased with increasing cohesive clay and EPS content, when these contents were below 2.8 vol% and 0.05 weight%, respectively. Above these limits, bedform migration and bed material transport was not detectable by the instruments in the study area. These limits are consistent with recently conducted sand-clay and sand-EPS laboratory experiments on bedform development. This work has important implications for the circumstances under which existing sand-only bedform migration transport formulae may be applied in a mixed sand-clay environment, particularly as 2.8 vol% cohesive clay is well within the commonly adopted definition of 'clean sand'.

Keywords: Bedform migration, Sediment transport, Mixed cohesive clay-sand, Physical and biological cohesion, Current and wave forcing, Tidal flats.

Abbreviations

3D-ARP	3D Acoustic Ripple Profiler (bed topography scanner)
ADV	Acoustic Doppler Velocimeter (single point current meter)
EPS	Extracellular Polymeric Substances (biologically produced cohesive material)
vol%	Volumetric percentage
wt%	Weight percentage

1. Introduction

Sediment transport models are essential tools for managing coastal morphological change, maintaining navigation channels and understanding the impacts of climate-induced habitat change in coastal and estuarine environments (Cowell *et al.*, 1995; Davies and Thorne, 2008; Amoudry and Souza, 2011; Jones *et al.*, 2013; Souza and Lane, 2013). Many of these environments are dominated by mixtures of sand and mud (Flemming, 2002; Waeles *et al.*, 2008). While reasonably accurate sediment transport predictors are available for pure sands, a knowledge gap exists for the behavior of mixed sediments composed of natural cohesive mud (clay and silt) and non-cohesive sand (Souza *et al.*, 2010; Amoudry and Souza, 2011; Manning *et al*, 2011; Spearman *et al.*, 2011; Aldridge *et al.*, 2015).

Mixtures of cohesive mud and sand have an increased critical shear stress for erosion compared to pure sand or mud (Mitchener and Torfs, 1996; Panagiotopoulos *et al.*, 1997; Jacobs *et al.*, 2011). The transition from erosion dominated by non-cohesive sand to cohesive clay has been found to occur at 3-5% clay (van Ledden *et al.*, 2004). In addition to the physical cohesion caused by electrostatic bonds between clay minerals, mixed sediments are also affected by biogenic cohesion, which results from the production of extracellular polymeric substances (EPS) by microphytobenthos and larger benthic organisms (Paterson and Black, 1999; van de Koppel *et al.*, 2001; Black *et al.*, 2002; Winterwerp and van Kesteren, 2004; Wotton, 2004; Tolhurst *et al.*, 2009).

Knowing the rate of migration of sedimentary bedforms, such as ripples and dunes, in coastal and estuarine environments is important in determining the bed material transport rate in sediment transport models (*e.g.*, Hubbell, 1964; Simons, 1965; van Rijn, 1984, 2006; van den Berg, 1987; Hoekstra *et al.*, 2004). These models may prove to be inaccurate if the bedform migration rates differ in mixed sand-mud and non-cohesive, mud-free sand (Amoudry *et al.*, 2009; Amoudry and Souza, 2011). Improvements in model predictions, or at least better insights into the range of conditions to which these models are relevant, should be possible by investigating the relationship between hydrodynamic forcing and bedform migration rate for mixed cohesive sediment.

Laboratory experiments and field measurements have demonstrated that bedforms can be inhibited from forming (Hagadorn and McDowell, 2012) and stabilized once formed (Grant *et al.*, 1986), due to biological cohesion from Extracellular Polymeric Substances (EPS) produced by benthic organisms. Recent laboratory experiments using mixed cohesive and non-cohesive sediment, and with added bacterial polymers as a proxy for natural biogenic stabilization, have shown that the dimensions of sedimentary bedforms decrease with increasing bed clay fraction and that the development rate of the bedforms is reduced by both physical and biological cohesion (Baas *et al.*, 2013; Malarkey *et al.*, 2015; Schindler *et al.*, 2015; Parsons *et al.*, 2016). These authors also showed that the clay and EPS were selectively entrained into suspension while ripples and dunes formed and migrated on the bed. This entrainment process of clay and EPS has been referred to as winnowing (*e.g.*, Lisle and Hilton, 1992; Harris *et al.*, 1993).

Winnowing in the freshwater experiments of Baas *et al.* (2013) and Malarkey *et al.* (2015) and in the seawater experiments of Schindler *et al.* (2015) and Parsons *et al.* (2016) caused the bedforms to migrate as if they were composed of clean sand, due to the reduction in bed clay and EPS content, despite their reduced development rate.

Bed mud content and biological production of EPS can be affected by the magnitude of the bed shear stress. Low stress promotes biological production and mud deposition, which has been proposed as an explanation for ripple stabilization in the field (Friend *et al.*, 2008), whereas high stress winnows cohesive material and provides poor conditions for microbial growth (van de Koppel *et al.*, 2001). Friend *et al.* (2008) found that a microalgal bloom coinciding with neap tides was sufficient to stabilize ripples on tidal flats for a period of four weeks. The influence of bed shear stress may lead to switching between alternate stable seabed states of cohesive erosion-resistant beds with well-developed biofilms and non-cohesive mobile beds, in environments with varying bed shear stress (van de Koppel *et al.*, 2001).

Sediment transport by the movement of current-generated bedforms on beds comprising biologically active mixtures of sand and mud is assumed to be controlled by the migration rate and the height of the bedforms, similar to bed material transport in pure sand (Hubbell, 1964; van den Berg, 1987). However, the cohesive forces within the bed might affect the bed material transport rate, as a few percent of clay and less than 0.1 wt% of EPS can be sufficient to significantly slow bedform growth (Baas *et al.*, 2013; Malarkey *et al.*, 2015). The migration rate of current ripples in clean sand and silt for unidirectional currents has been studied in laboratory flumes (van den Berg and van Gelder, 1993; Baas *et al.*, 2000). Here, these experimental data are compared with the migration rate of similar bedforms in mixed sand-mud on natural intertidal flats in the Dee Estuary, near West Kirby, northwest England. The principal aims of this field-laboratory comparison were: (1) to extend the widely used relationship between bedform migration rate and bed material transport rate (Hubbell, 1964;

van den Berg, 1987) from laboratory to field conditions, and; (2) to determine the effect of cohesion by clay and EPS on bed material transport rate.

In this paper, we first describe a method for relating the field-based hydrodynamic data to bedform migration rate and bed material transport rate, correcting for the influence of waves on the bed shear stress. Then, the calculated bedform migration rates for the mixed sand-mud in the field are compared to laboratory flume data for pure sand with a similar grain size. Thereafter, a multiple linear regression analysis is applied to quantify the effect of bed cohesion on the bed material transport rate in relation to bed shear stress. Finally, recommendations are made for sediment transport modelling in mixed cohesive sediment.

2. Relating current bedform migration rate to bed material transport rate

Current-generated bedforms migrate in the direction of the hydrodynamic forcing by erosion of sediment from the low-angle slope of the upstream face and deposition by avalanching on the steeper downstream face of these bedforms (Deacon, 1894; Sternberg, 1967; Allen, 1968; Smyth and Li, 2005). The rate of migration of these bedforms depends on the sediment characteristics, chiefly its grain size, the size of the bedforms, and the hydrodynamic forcing (*e.g.*, van den Berg, 1987). Successive bed profile measurements with a known time interval can be used to calculate the migration rate of bedforms (Sternberg, 1967; van den Berg, 1987; Bell and Thorne, 1997; Hoekstra *et al.*, 2004; Masselink *et al.*, 2007). The bed material transport rate can then be calculated from this migration rate, if the size, geometry, and porosity of the bedforms are known (Hubbell, 1964; Simons, 1965; van den Berg, 1987; Hoekstra *et al.*, 2004). This procedure is described below, after introducing the hydrodynamic forcing that drives bedform migration.

2.1. Hydrodynamic forcing

In shallow marine environments, submerged bed surface sediment moves predominantly by the combined forces of currents and waves. These driving forces are often represented by a dimensionless bed shear stress or mobility parameter, such as the Shields parameter, θ, which accounts for the diameter of the sediment grains and the relative density of the sediment in water (Shields, 1936; Soulsby, 1997; Paphitis, 2001):

$$\theta = \frac{\tau}{(\rho_s - \rho) g D_{50}} \qquad (1)$$

where τ is the total bed shear stress, ρ_s is the sediment density, ρ is the water density, g is the acceleration due to gravity, and D_{50} is the median grain diameter. Equation 1 can be applied to waves (θ_w and τ_w), currents (θ_c and τ_c), and combined flows ($\theta_{\max}$ and $\tau_{\max}$. Appendix A provides a list of at the parameters used in the analysis). The Shields parameter can incorporate the contributions of skin, or sediment grain, friction and form drag in the bed shear stress (Soulsby, 1997). The skin friction component of the shear stress determines the movement of sediment particles on the bed, and is therefore important for the development and migration of bedforms and the bed material transport rate. The form drag component of the shear stress, caused by bedforms acting as roughness elements, is more important for the transport of suspended sediment higher up in the flow (Soulsby, 1997). The notation θ' is used for mobility parameters that are based only on the skin friction contribution in the bed shear stress. Plotting the bedform migration rate against skin friction mobility parameter allows a comparison to be made between these parameters for different sediment sizes (Baas *et al.*, 2000).

The maximum bed shear stress in combined wave-current flow is not a straightforward sum of the unidirectional and oscillatory components, as the interactions between the waves and the current in the near-bed wave boundary layer are non-linear. Various models that account for these non-linear interactions have been introduced to calculate bed shear stresses in combined wave and current flows (*e.g.*, Grant and Madsen, 1979; Soulsby *et al.*, 1993; Madsen, 1994; Soulsby and Clarke, 2005; Malarkey and Davies, 2012). These models are typically based on the assumption of a simple two-layer eddy viscosity profile (Grant and Madsen, 1979), with a number of subsequent refinements over the years. Madsen (1994) extended the model of Grant and Madsen (1979) to account for wave spectra. These models differ in the degree of non-linearity within the wave boundary layer. The theoretically derived Grant and Madsen (1979) and Madsen (1994) iterative models are the most non-linear, because the eddy viscosity is scaled on the peak stress in the wave cycle. The Soulsby and Clarke (2005) non-iterative model is the least non-linear, because the eddy viscosity is scaled on an effective velocity. The Soulsby and Clarke (2005) model output is closest to available experimental data. The non-iterative Malarkey and Davies (2012) model, based on the Soulsby and Clarke (2005) model, which represents a compromise between the two extremes of the purely theoretical strong non-linearity and the weak non-linearity associated with experimental data, agrees well with numerical modelling results (Malarkey and Davies, 2012) and has been chosen for the present study.

2.2. Migration rate of current-generated bedforms

Sediment transport is commonly parameterized in terms of dimensionless quantities (Yalin, 1977), for example the Shields parameter, as in equation 1. Baas *et al.* (2000) proposed a simple power law relationship between experimental data on the bedform migration rate, u_b, for current ripples and the skin-friction related Shields parameter, θ', as shown in Figure 1:

$$u_b = \alpha\theta'^{\beta} \quad (2)$$

where α (m s^{-1}) and β are coefficients that vary with the size of the sediment on the bed (Baas *et al.*, 2000). Baas *et al.* (2000) showed that α and β increase with increasing median grain diameter. Hence, bedforms composed of coarser grains migrate faster than bedforms composed of finer grains at the same Shields parameter as seen in Figure 1.

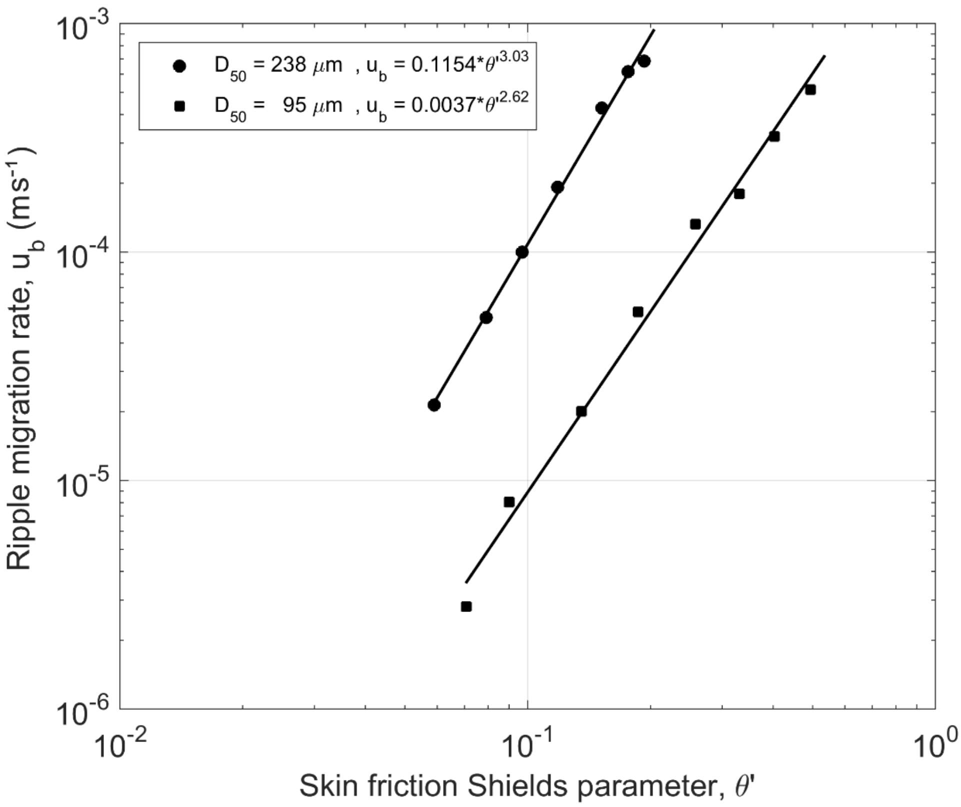

Figure 1: Empirical relationships between the migration rate of equilibrium current ripples and the skin-friction Shields mobility parameter for two median grain sizes: 238 µm and 95 µm (modified after Baas *et al.* (2000)). The raw data have been re-processed using the same roughness-length specification of skin friction as for the field data ($z_0 = D_{50}/12$).

2.3. Bed material transport rate

Richardson *et al.* (1961) assumed a triangular bedform shape in vertical cross-sections parallel to the flow direction to propose the basic equation for the transport rate of bed material through bedform migration:

$$q_b = 0.5\,(1 - P)\,u_b\,\eta \qquad (3)$$

where q_b is the volume transport rate per unit width, η is the bedform height and P is the porosity of the bed. However, most ripples and dunes do not have a perfectly triangular shape in cross-section. Therefore, van Rijn (2006) replaced the factor 0.5 in equation 3 with a bedform shape factor, f, which has been shown to be approximately 0.6 for current ripples and dunes (van den Berg, 1987; Hoekstra *et al.*, 2004; Baas *et al.*, 2011). Equation 3 also assumes that mean bedform height does not change during bedform migration (*i.e.*, the bedforms are in perfect equilibrium with the flow conditions), and losses or gains of sediment from the sampling area by resuspension or deposition are absent (van den Berg, 1987). Hubbell (1964) proposed a factor, K, to account for sediment loss by resuspension and sediment gain by deposition. In order to calculate the mass transport rate, Q_b, the volume transport rate, q_b, needs to be multiplied by the sediment density (van Rijn, 1984, 2006; van den Berg, 1987):

$$Q_b = K\rho_s(1 - P)fu_b\eta \qquad (4)$$

Equation 4 thus accounts for variations in bedform shape through f, and for net resuspension and net deposition through K.

3. Methods

3.1. Field site and experimental setup

Hydrodynamic and sediment dynamic data were collected from three sites on an intertidal flat in the Dee Estuary near West Kirby, United Kingdom (Figure 2). The Dee Estuary is a hypertidal, funnel-shaped estuary in the eastern Irish Sea between England and Wales, bifurcated into two main channels at the mouth. The estuary is tidally dominated, with a 7-8 m mean spring tidal range at Hilbre Island. Hilbre Island separates Hilbre Channel from intertidal flats to the east (Figure 2). These tidal flats significantly distort the tide and increase the tidal asymmetry, causing flood dominance that has resulted in the accretion of fine-grained sediment (Moore *et al.*, 2009). Waves are mainly generated locally within Liverpool Bay, with northwesterly waves having the largest influence on the sedimentary processes in the Dee Estuary (Brown and Wolf, 2009; Villaret *et al.*, 2011). Swell from the North Atlantic is unable to reach the Dee Estuary. Sediment in the Dee Estuary is therefore derived mainly from the Irish Sea, with a small additional contribution from local cliff erosion (Halcrow, 2013). Sediment in the lower intertidal areas is mainly sandy, becoming muddier towards the landward limit of the estuary (Halcrow, 2013).

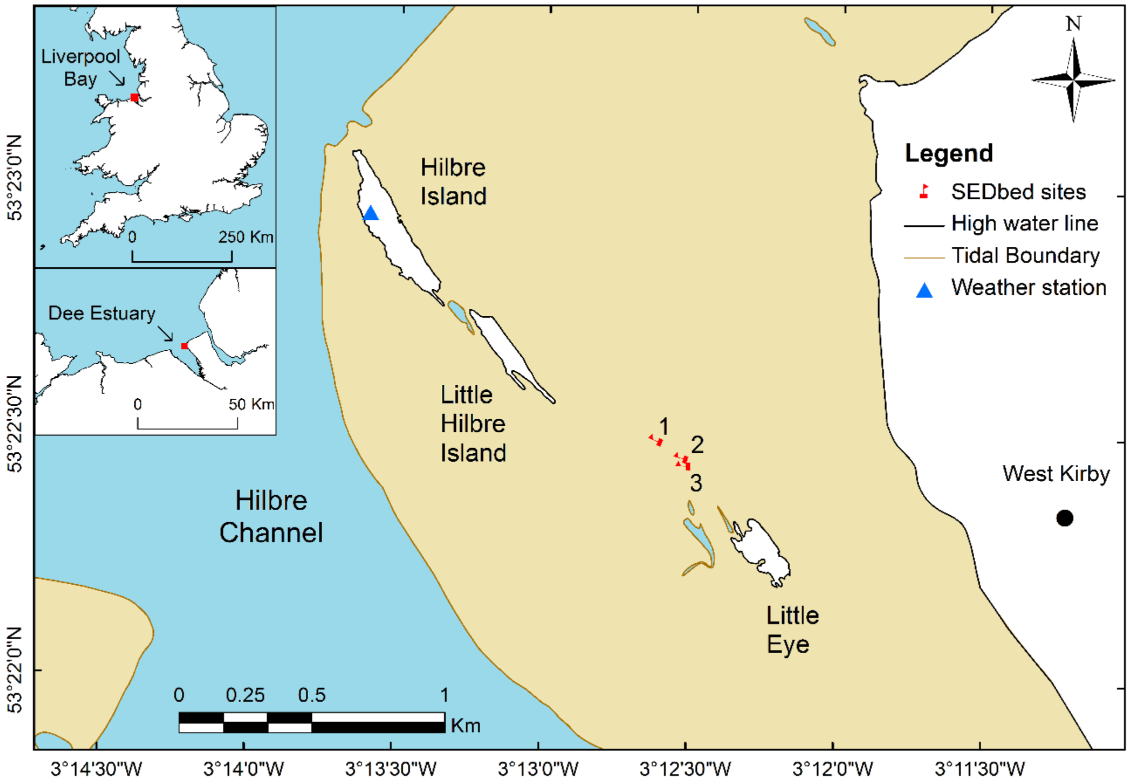

Figure 2: Map of the Dee Estuary, United Kingdom, showing the three deployment sites of the SEDbed frame (the direction of the flags on the red markers indicate the orientation of the SEDbed frame) on the intertidal flat (in light brown) between West Kirby and the subtidal Hilbre Channel (in blue) (map contains Ordnance Survey data © Crown copyright and database 2013).

Three sites on the intertidal flat near West Kirby were selected (Figure 2) and studied over a spring-neap cycle in May and June 2013 in order to cover a range of mixtures of sand and mud. A suite of instrumentation on the National Oceanography Centre's SEDbed frame was deployed at each site consecutively to measure the currents, waves, bedforms, and suspended sediment (Figure 3). Bed samples were collected and analyzed for cohesive clay and biological content. This study uses hydrodynamic data, collected with an Acoustic Doppler Velocimeter (ADV), measurements of water properties from a Conductivity, Temperature and Density (CTD) system, and seabed topography data provided by a 3D Acoustic Ripple Profiler (3D-

ARP; Figure 3; Table 2), with reference to the cohesive content of the sea bed. The 3D-ARP is a dual axis, mechanically rotated, pencil beam scanning sonar operating at 1.1 MHz, which images a circular area of the seabed (Thorne and Hanes, 2002; Marine Electronics, 2009). During the deployment at Site 1, 21-24 May 2013, waves dominated as neap tide progressed towards spring tide and the wind ranged from moderate breezes up to gale force (Beaufort scale 4-8; 5.8 - 17.6 m s^{-1}). The wind reduced on 24 May and remained calm for the rest of the fieldwork. The period at Site 2, 24-29 May 2013, was dominated by currents, as the tide progressed to the peak of spring tide and then reduced. During the deployment at Site 3, 29 May to 4 June 2013, the maximum current strength reduced towards neap tide. Table 1 summarizes the hydrodynamic conditions during the field deployment.

Table 1: Summary of the hydrodynamic conditions.

Site	Date range	Hydrodynamic Conditions
1	21-24 May 2013	Largely wave-dominated, as neap tide progressed towards spring tide with near gale force winds
2	24-29 May 2013	Current-dominated, as the tide progressed to the peak of spring tide and then reduced
3	29 May - 4 June 2013	Weak hydrodynamics, current strength reduced towards neap tide and low wave forcing

The sites were within 140 m of each other, differing in bed elevation by 0.19 m. The tide, wind, and wave forcing varied over the record at the three sites, covering a full spring-neap cycle from neap tide to neap tide. The migration rates and bed material transport rates of small-scale bedforms in biologically active, mixed sand-mud, were determined and compared with data from laboratory bedforms in pure sand (Baas *et al.*, 2000), mixed sand-clay (Baas *et al.*, 2013) and mixed sand-EPS (Malarkey *et al.*, 2015).

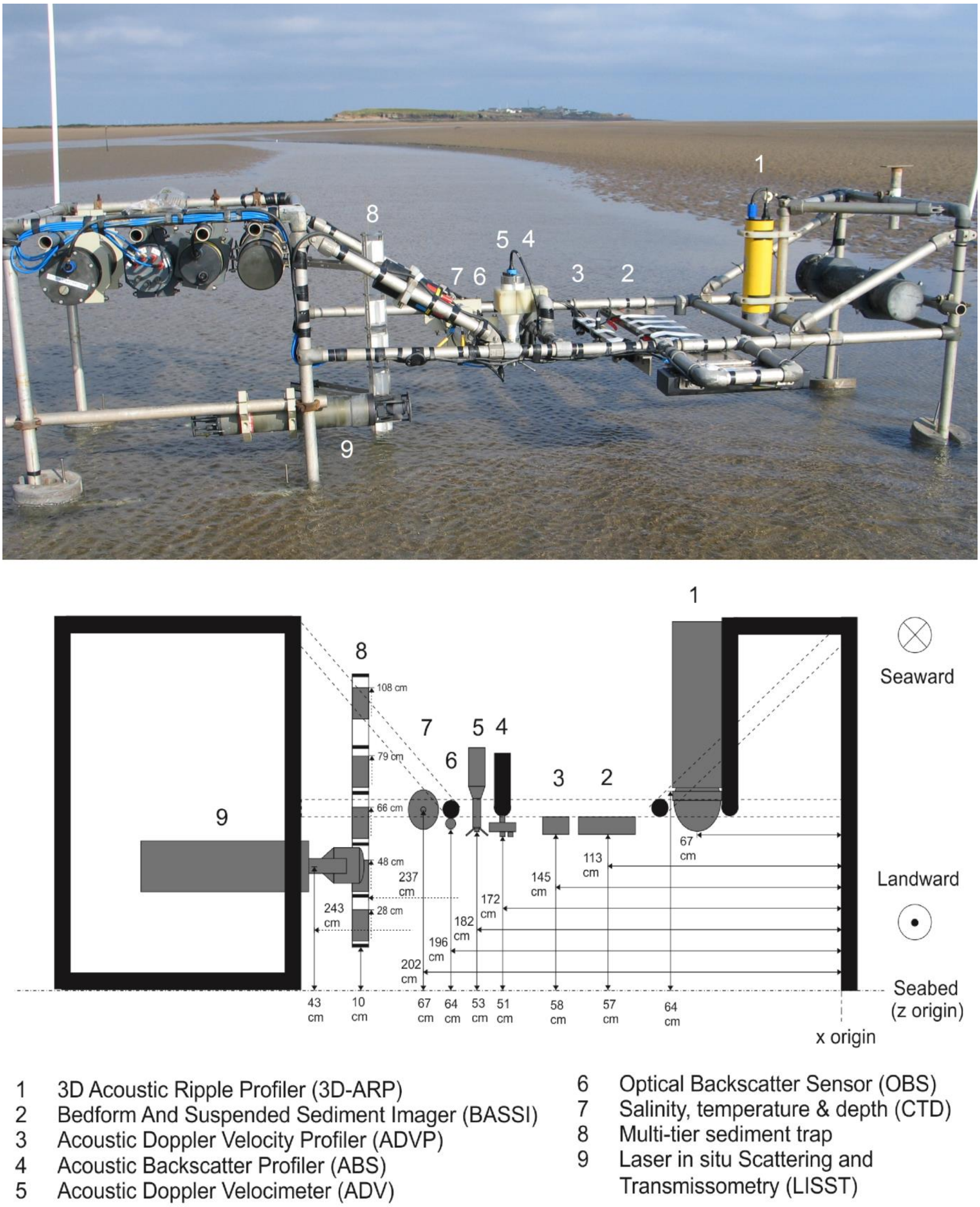

Figure 3: Instrument frame SEDbed at Site 2, looking seaward towards Little Hilbre and Hilbre Island (top), and diagram of instruments on frame (bottom). Initial heights above the sediment bed are shown, with horizontal distance relative to the edge of the frame.

Table 2: Specifications and settings of instruments used in this study.

No. [a]	Instrument	Specifications and settings	
1	Marine Electronics 3D Sand Ripple Profiling Logging Sonar (3D-Acoustic Ripple Profiler)	Swath angle:	±75° to vertical
		Vertical resolution:	0.003 m
		Angle resolution:	0.9°
		Range:	2.5 m
		Sample interval:	30 minutes
5	SonTek Hydra-ADV	Velocity resolution:	0.001 m s^{-1}
		Velocity accuracy:	± 1%
		Range to bed resolution:	0.0001 m
		Pressure resolution:	0.008 bar
		Recording rate :	8 Hz
		Burst Length:	55 minutes
		Sample interval:	60 minutes
7	SeaBird SBE16+ CTD, v. 1.8c	Pressure resolution:	0.001 bar
		Pressure accuracy:	0.008 bar
		Temperature precision:	0.0001 °C
		Temperature accuracy:	0.005 °C
		Conductivity precision:	0.00005 S m^{-1}
		Conductivity accuracy:	0.0005 S m^{-1}
		Sample interval:	1 minute

[a] Numbering corresponds to Figure 3.

3.2. Bed sample analysis

A total of fourteen bed samples were collected during low slack water from the three sites (Figure 2), with the objective to relate the bedform migration rate to the clay content of the substrate. Sediment taken from the top 1-2 cm below the crests and troughs of the bedforms, within one meter of the SEDbed frame, was homogenized for each sample. The bed clay, silt, and sand volume fractions for each sample were determined, using the Malvern 2000 Laser Particle Sizer at Bangor University. Clay particles are defined as particles of size below 3.9 μm, silt in the range 3.9-62.5 μm and mud particles (clay and silt) of size less than 62.5 μm (Wentworth, 1922). The mean D_{50} of the bed samples was 227 μm.

X-ray powder diffraction (XRD) data (using standard methodology for bulk sediment analysis: Moore and Reynolds (1997)), based on seven randomly selected bed samples taken during the fieldwork, show that the mud fraction at the field site contained 36% ± 4% clay minerals by volume, where 4% denotes the standard deviation of the mean. In decreasing order of abundance, the clay mineral assemblage comprised illite, chlorite, and kaolinite, where illite is the most cohesive clay mineral and chlorite is the least cohesive clay mineral (*e.g.* Mehta, 2014). This 36 vol% based on the mineralogy is inferred to represent the cohesive fraction within the mud more accurately than the particle size limit for the clay fraction, as the remaining 64 vol% was dominated by non-cohesive quartz and feldspar. The bed mud content values from the 14 bed samples were converted to cohesive clay content using a correction factor based on the XRD-derived fraction, which yielded cohesive clay fractions in the range 0.6 to 5.4 vol%. These values are referred to as the cohesive clay fraction from here onwards. As the bed sediment was dominated by quartz, a density value of 2650 kg m^{-3} was used in the computations of the Shields stress parameters.

Additional bed surface samples were collected in the vicinity of the three sites for the determination of EPS content, as a measure of the biologically cohesive materials in the sediment. The EPS fraction is represented by the total carbohydrate content of the sediment by dry weight (Underwood *et al.*, 1995) determined using the standard Dubois assay (Dubois *et al.*, 1956). The EPS fractions of these bed samples were in the range 0.02 to 0.30 wt%. These samples were also analyzed for bed mud content, using the Malvern 2000, and then corrected using the XRD factor to obtain the cohesive clay content values.

3.3. Bedform migration data

While 1D cross-correlation techniques have been used previously to determine bedform migration (Smyth and Li, 2005; Masselink *et al.*, 2007), here these are generalized by using 2D techniques (Giachetti, 2000; Sutton *et al.*, 2009). 1D methods only resolve the bedform migration along a single axis, and are thus best suited to cases where the waves and currents are co-linear and the bedforms are straight crested. By using 2D cross-correlation, waves and currents at any angle and three-dimensional bedforms can be considered. The bedform migration rate was calculated from the spatial difference between successive half-hourly 3D-ARP bed elevation scans, determined by 2D cross-correlation. The distance migrated between two scans is divided by the time between scans to get the migration rate. The 3D-ARP data did not show any change in the large-scale bedform morphology during the deployment. However, prior to the 2D cross-correlation, bed slope was removed from each scan using orthogonal least squares regression (Borradaile, 2003), also known as major axis regression. This method assumes that all the variables have errors, in contrast to standard linear regression, which assumes that only the dependent variable has errors (Borradaile, 2003). The 3D-ARP scans used for the 2D cross-correlation were sub-sampled over areas of 0.5×0.5 m to remove the potential influence of scour around the legs of the instrument frame on the bedform dynamics. The 2D cross-correlation of the half-hourly scan pairs yielded 143 bedform migration rates. The 3D-ARP data were processed to a spatial resolution of 0.005 m. For the half-hourly sampling interval, the minimum ripple migration rate detectable was 2.8×10^{-6} m s^{-1}. All migration rates at and below this limit were excluded from the regression model. An orthogonal least squares regression model was used to fit the bedform migration rate to the Shields parameter.

The error of the cross-correlation of bedform migration distance was estimated from the peak normalized cross-correlation value, $\rho_{12}(\tau^*)$, the bandwidth of the data, B, and the record length, T_{rl}, in the vector direction of the 2D lag (to reduce the problem from two dimensional to one dimensional). The estimate of the normalized RMS error, E_{nrms}, for the peak correlation lag, τ^*, is (Bendat and Piersol, 1986):

$$E_{nrms} = \frac{1}{\sqrt{2BT_{rl}}}\left[1 + \frac{1}{\rho_{12}^2(\tau^*)}\right]^{0.5} \tag{5}$$

where the normalized cross-correlation function, $\rho_{12}(\tau^*)$, is:

$$\rho_{12}(\tau^*) = \frac{R_{12}(\tau^*)}{\sqrt{R_{11}(0)R_{22}(0)}} \tag{6}$$

and $R_{12}(\tau^*)$ is the cross-correlation function, $R_{11}(0)$ is the autocorrelation function for scan 1 at zero lag, and $R_{22}(0)$ is the autocorrelation function for scan 2 at zero lag. The normalized root-mean square (RMS) error was used to estimate the standard deviation, $\sigma(\tau^*)$, and the 95% confidence interval, C, (Bendat and Piersol, 1986):

$$\sigma(\tau^*) = \frac{0.93}{\pi B}\sqrt{E_{nrms}} \tag{7}$$

$$C = 1.96\sigma(\tau^*) \tag{8}$$

where the bandwidth, B, is the wave number of the lag interval, which in the present study is the inverse of the horizontal resolution of 0.005 m. The confidence intervals were divided by the time intervals to determine the migration rate errors.

3.4. Hydrodynamic data analysis

The ADV recorded the water velocity at 0.37 m above the seabed and the water pressure at 0.53 m above the seabed, with a sampling rate of 8 Hz (Table 2; Figure 3). Pressure data from the ADV and CTD were corrected using an air pressure time series from the weather station on Hilbre Island, and then converted to water depth values and corrected for the instrument height from the seabed. Seawater density, water depth and sound velocity were calculated using the IOC-UNESCO Gibbs-SeaWater Oceanographic Toolbox (v3.03; http://www.teos-10.org (McDougall and Barker, 2011)). Tidal currents were extracted from the ADV data by applying a 5-minute running mean. The ADV time series was then processed in 30-minute windows, matching the interval used to collect the bedform migration rate data, to extract current, wave, and combined flow bed shear stress values, using the procedure described below.

The depth-averaged velocity was calculated using the two-layer logarithmic model of Malarkey and Davies (2012), in which roughness accounted for both skin friction and bedform drag. Roughness length, z_0, was determined from the bedform dimensions obtained with the 3D-ARP and from the mean D_{50} of the bed sediment samples for each site (227 μm), for this purpose ($z_0 = \eta^2/\lambda + D_{50}/12$, where η and λ are the bedform height and length; (Soulsby, 1997)).

Sea surface wave parameters were obtained from the pressure (P) and horizontal velocity (components U and V) spectra using the PUV method (Gordon and Lohrmann, 2001). This method corrects for the instrument height above the bed using linear wave theory, and also accounts for the current-induced Doppler shift. Pressure, horizontal velocity, and depth-averaged velocity data were used to calculate the wave number, the wave attenuation factor and the wave pressure spectrum, resulting in the surface elevation spectrum (Fenton and McKee, 1990; Gordon and Lohrmann, 2001; Bolaños *et al.*, 2012). As the field dataset lacks direct measurements of wavelength, the wave number was approximated by applying the

Newton-Raphson iteration method to the dispersion equation (Fenton and McKee, 1990; Soulsby, 1997, 2006; Wiberg and Sherwood, 2008). This method accounts for the effect of currents, including the angle between the wave and current direction, φ (Fenton and McKee 1990; Soulsby, 1997). Wave height and wave period were determined from the statistical moments of the surface elevation spectrum. The time-series of the wave period was de-spiked separately for each tidal inundation period, removing points greater than four standard deviations from a mode filter value and replacing these with the mean. Again using linear wave theory, the significant wave height, H_s, peak wave period, T_p, and water depth, h, were then used to calculate the bottom orbital velocity amplitude, u_w, for subsequent bed shear stress calculations (Soulsby, 1997, 2006).

Prior knowledge of the wave parameters is required to calculate the depth-averaged current velocity in combined flow. Therefore, an iterative procedure was used to determine the depth-averaged current velocity, $\langle u \rangle$, and the wave parameters, H_s, T_p and u_w. An initial estimate of the depth-averaged current velocity was made, assuming a logarithmic profile and using the ADV mean current velocity, before iterating between the two-stage logarithmic model (Malarkey and Davies, 2012) and the PUV method (Gordon and Lohrmann, 2001) until the difference in depth-averaged velocity converged.

The combined maximum wave and current bed shear stress, τ'_{max}, was calculated with the Malarkey and Davies' (2012) model, using their stronger non-linear interaction option. In this case, the roughness length, z_0, for the bed shear stress calculation was based on skin friction, $z_0 = D_{50}/12$, using D_{50} = 227 μm (Soulsby, 1997). In addition to the maximum bed shear stress, τ'_{max}, the model also produces a combined-mean stress and a combined-wave stress together with corresponding linear stresses: current-only, τ'_c; wave-only, τ'_w; and a maximum linear stress, $\tau'_{\mathrm{max}l}$, which would result if the process was a completely linear vector addition of the current and wave stresses without any interaction (see appendix B). The skin friction Shields parameter, θ'_{max}, was calculated for τ'_{max} based on equation 1, where a density value of 2650 kg m^{-3} was used as the bed sediment was dominated by quartz. θ'_{max} was then used to compare with the bedform migration rates and bed material transport rates. In the absence of waves, $\theta'_{max} = \theta'_c$. The original velocity data of Baas *et al.* (2000) were re-processed using the same roughness length specification of skin friction as for the field data ($z_0 = D_{50}/12$), so that all bed shear stress calculations in the present study were based on the same procedure.

3.5. Bed material transport rate

The bedform migration rates were derived from the 3D-ARP data via 2D cross-correlation, as described in Section 3.3, and the bedform dimensions were computed using the zero-crossing method after correction for the bedform orientation using a Radon transform and matrix rotation (Jafari-Khouzani and Soltanian-Zadeh, 2005; van der Mark *et al.*, 2008). These bedform migration rates were used in equation 4 to calculate bed material transport rate. For the purpose of verifying if the studied bedforms in the Dee Estuary had reached equilibrium dimensions, the measured bedform dimensions were compared with the equilibrium ripple dimensions for D_{50} = 238 μm, measured by Baas (1999) (height η_{eq} = 0.017 m; length, λ_{eq} = 0.141 m), and ripple heights and lengths predicted by the empirical relationships of Soulsby *et al.*, (2012; η_{eq}, = 0.019 m and λ_{eq}, = 0.153 m, for D_{50} = 227 μm) from the following equations:

$$\eta_{eq} = D_{50} 202 D_*^{-0.554} \tag{9}$$

$$\lambda_{eq} = D_{50}(500 + 1881 D_*^{-1.5}) \qquad \text{for } 1.2 < D_* < 16$$

where D_* is the dimensionless grain diameter, $D_* = D_{50}[g(s-1)/v^2]^{1/3}$, D_{50} is the median grain diameter, $s = \rho_s/\rho$ is the relative density of the sediment (ρ_s is taken to be that of quartz, 2650 kg m^{-3}) and v is the kinematic viscosity of water.

The shape factor, f, the sediment loss-gain factor, K, and the sediment density, ρ_s, in equation 4 were kept constant at 0.6, 1, and 2650 kg m^{-3}, respectively (van den Berg, 1987; van Rijn, 2006). The shape factor value assumes that all the laboratory flume and field bedforms in this work have a cross-section similar to current ripples and dunes. Approximating the mean shape factor and its standard deviation, based on the entire 3D-ARP bedform dataset, gave a value of $f = 0.52 \pm 0.09$, which agrees reasonably well with the value of 0.6 used here and in previous studies (van den Berg, 1987; van Rijn, 2006). The sediment loss-gain factor of 1 assumes no significant loss or gain of bed sediment. A porosity of 0.4 was used for both the laboratory and field sand, which is a compromise between loosely packed and tightly packed natural sand (*e.g.*, Allen 1984). It has been assumed that the change in porosity due to the presence of mud (mostly << 15 vol%) was small, since the silt component is taken up into suspension as the bedforms migrate.

4. Results

4.1. Bed composition

A linear fit was used to describe the changes in bed cohesive clay fraction at Sites 1 and 2, which were dominated by wave action and spring tide, respectively (Figure 4). A second-order polynomial fit was used to describe the temporal trend in bed cohesive clay fraction at Site 3, where the tide progressed to neap and the wave stress was low (Figure 4). While the discontinuities in the fits between sites provide evidence of spatial variation, this difference is assumed to have a small effect on the results. Waves are known to enhance the winnowing process (Baas *et al.*, 2014) and high wave stress was only present at Site 1. Site 2 was at the lowest bed elevation and includes the peak of spring tide. At Site 3, there was a trend of increasing bed cohesive clay content as the tide progressed from spring to neap at the end of the record (Figure 4). The tide dominated the bed composition, with the lowest bed cohesive clay content seen at Site 2 during spring tide and the increase of cohesive clay content at Site 3 with the progression of the tide to neap.

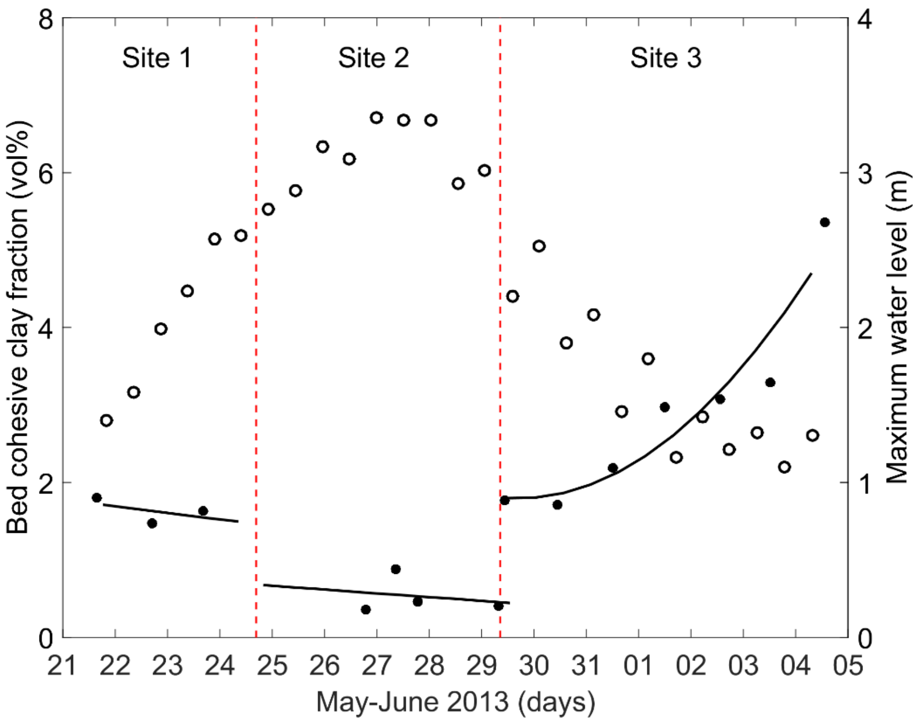

Figure 4: Time-series of bed cohesive clay fraction (●) and maximum tidal height (○) for the study period (only analyzed for particle size). A linear fit was used to describe changes in bed cohesive clay fraction at Sites 1 and 2, whereas a second-order polynomial fit was used to describe the temporal trend in bed cohesive clay fraction at Site 3. Bed cohesive clay fraction represents the total percentage of cohesive clay minerals within the sediment. The vertical dashed lines mark the times when the instruments were moved between sites.

The EPS fractions, from the sediment carbohydrate content analysis, are plotted against the cohesive clay fractions within the same samples in Figure 5. The thick grey lines represent the thresholds of bedform migration for a bed clay fraction of 2.5 vol%, based on Baas *et al.* (2013), and an EPS fraction of 0.063 wt%, based on Malarkey *et al.* (2015). Low EPS fractions correspond to low cohesive clay fractions (Sites 1 and 2) below the limits of Baas *et al.* (2013) and Malarkey *et al.* (2015) for bedform formation. High EPS fractions matched high cohesive clay fractions (Site 3), where bedform migration was found to be substantially reduced due to cohesion (Baas *et al.*, 2013; and Malarkey *et al.*, 2015). The scatter in the data shown in Figure 5 may be attributed to the patchiness of the EPS and cohesive clay across the sampled areas, inherent in biological processes. A robust linear regression line describes the relationship between bed EPS content and bed cohesive clay content ($R^2 = 0.41$, $p < 0.05$ and RMS error = 0.058, for $n = 20$):

$$e = 0.0105c + 0.0302, \tag{10}$$

where e and c are the weight and volumetric percentages of EPS and cohesive clay, respectively (Figure 5). Below, we assume that this simple linear relationship also applies to the bed samples for which no EPS data are available. From these data, the effects of physical and biological cohesion cannot be distinguished from each another, as the variation in EPS content is related to the variation in cohesive clay content. Therefore, the term ‘cohesive clay’ represents both physical and biological cohesion in this study.

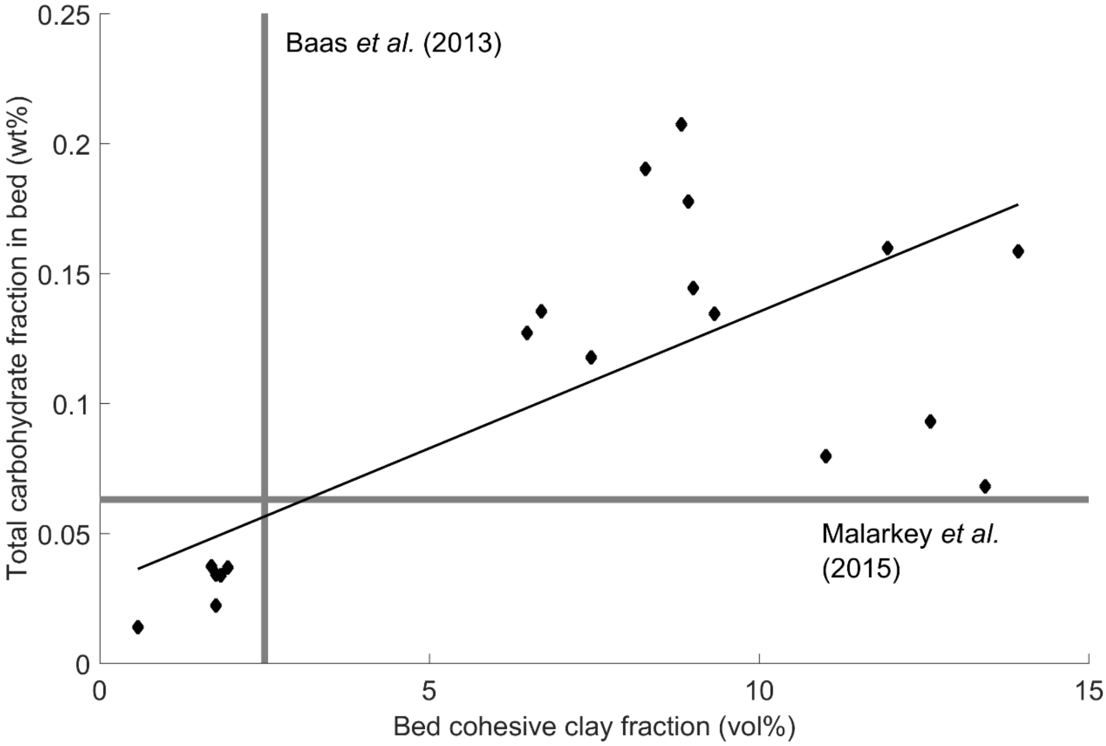

Figure 5: Total carbohydrate fraction (EPS) against bed cohesive clay fraction, derived from bed samples collected in the vicinity of Sites 1 to 3 (analyzed for EPS and particle size). The thick grey lines represent the thresholds of bedform migration for a bed cohesive clay fraction of 2.5%, based on Baas *et al.* (2013), and an EPS fraction of 0.063%, based on Malarkey *et al.* (2015). The values from Site 3 fall to the right of the Baas *et al.* (2013) line and above the Malarkey *et al.* (2015) line. The black line represents a robust linear regression fit ($R^2 = 0.41$, $p < 0.05$ and RMS error = 0.058, for $n = 20$, equation 10) between the cohesive clay and EPS values. In appendix C these data are plotted for total carbohydrate per unit volume for comparison with other work (Tolhurst *et al.*, 2005).

4.2. Flow forcing

During the study period in 2013, the tide advanced from neap to spring and back to neap (Figure 6a and 6b). The measurements at Site 1 were conducted during the transition from neap to spring tide, spring tide prevailed during Site 2, and Site 3 was sampled during the transition from spring to neap tide. North-westerly winds dominated when Site 1 was sampled, with wind conditions from moderate breezes up to gale force (Beaufort scale 4-8; 5.8 - 17.6 m s^{-1}). These high winds caused wave height to increase (Figure 6c), albeit modulated by the depth of the tidal flows (Brown, 2010; Friedrichs, 2011). The dominant wind-generated wave periods ranged from 2 to 12 seconds (Figure 6d). The strong winds at Site 1 generated wind-driven flow that increased the velocity magnitude of the flood tide, compared to the fair-weather conditions at Site 3, and prevented a clear slack water from occurring at high tide (tidal periods 4 to 6, Figure 6a, 6b). The bottom orbital amplitude velocity is shown in Figure 6e.

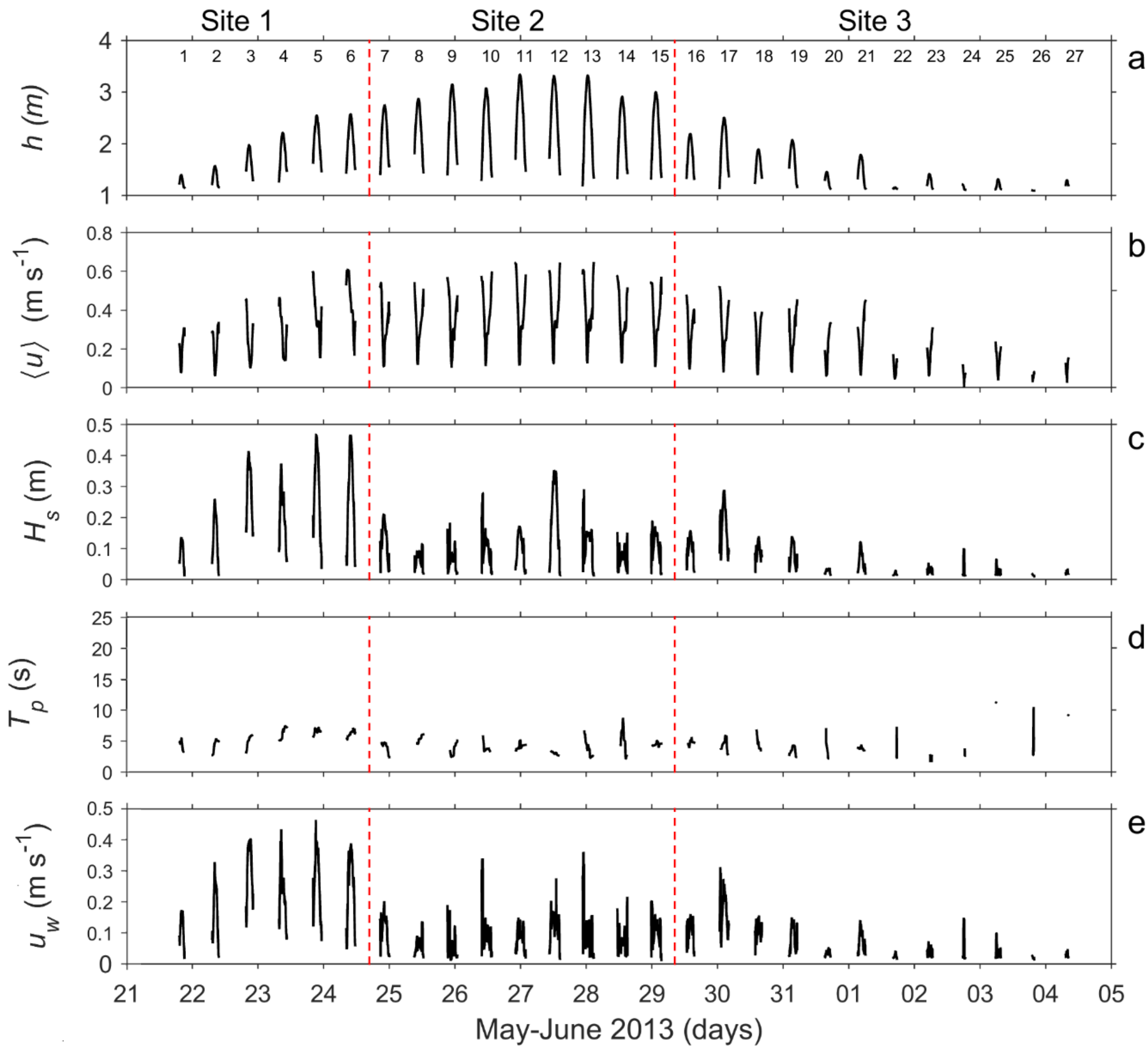

Figure 6: Times series of (a) water depth, *h*; (b) depth-averaged flow velocity (30 minute running mean), ⟨*u*⟩; (c) significant wave height, H_s; (d) peak wave period, T_p (smoothed to show trend); and (e) wave bottom orbital amplitude velocity, u_w. The vertical red dashed lines mark the times when the SEDbed frame was moved between sites. The data shown are for when the tidal flats were inundated with water above the height of the sensors, processed for a 30-minute window. The wave period data were filtered to show only the wind-generated waves of periods less than 25 seconds (USACE, 2002a). The numbers in (a) denote the tidal periods for reference.

Similar patterns in the bed shear stress data can be seen in Figure 7a to 7c. The wind-driven flow caused an increase in the current-only bed shear stress on 23-25 May, during tidal periods 4 to 6 (Figure 7a), when the wave bottom orbital velocities were highest (Figure 6e). Despite experiencing spring tide, the peak current-only bed shear stress for Site 2 was similar to that at Site 1 for tidal periods 11 to 13 (Figure 7a). Relatively weak currents dominated the neap tide at Site 3, resulting in low bed shear stresses (Figure 7a). Wave-only bed shear stresses were significant during the strong north-westerly wind conditions at Site 1 for tidal periods 2 to 6 (Figure 7b). The maximum bed shear stress, which combines current and wave bed shear stresses non-linearly (see equation B3, Appendix B), was dominated by the currents, except for Site 1, where waves dominated during tidal periods 3 to 6 (Figure 7c). By comparing τ'_{max} and $\tau'_{\mathrm{max}l}$ (the linear equivalent), it can be seen that the maximum stress was non-linear only at peak stresses, when there were strong waves at Site 1 (Figure 7c).

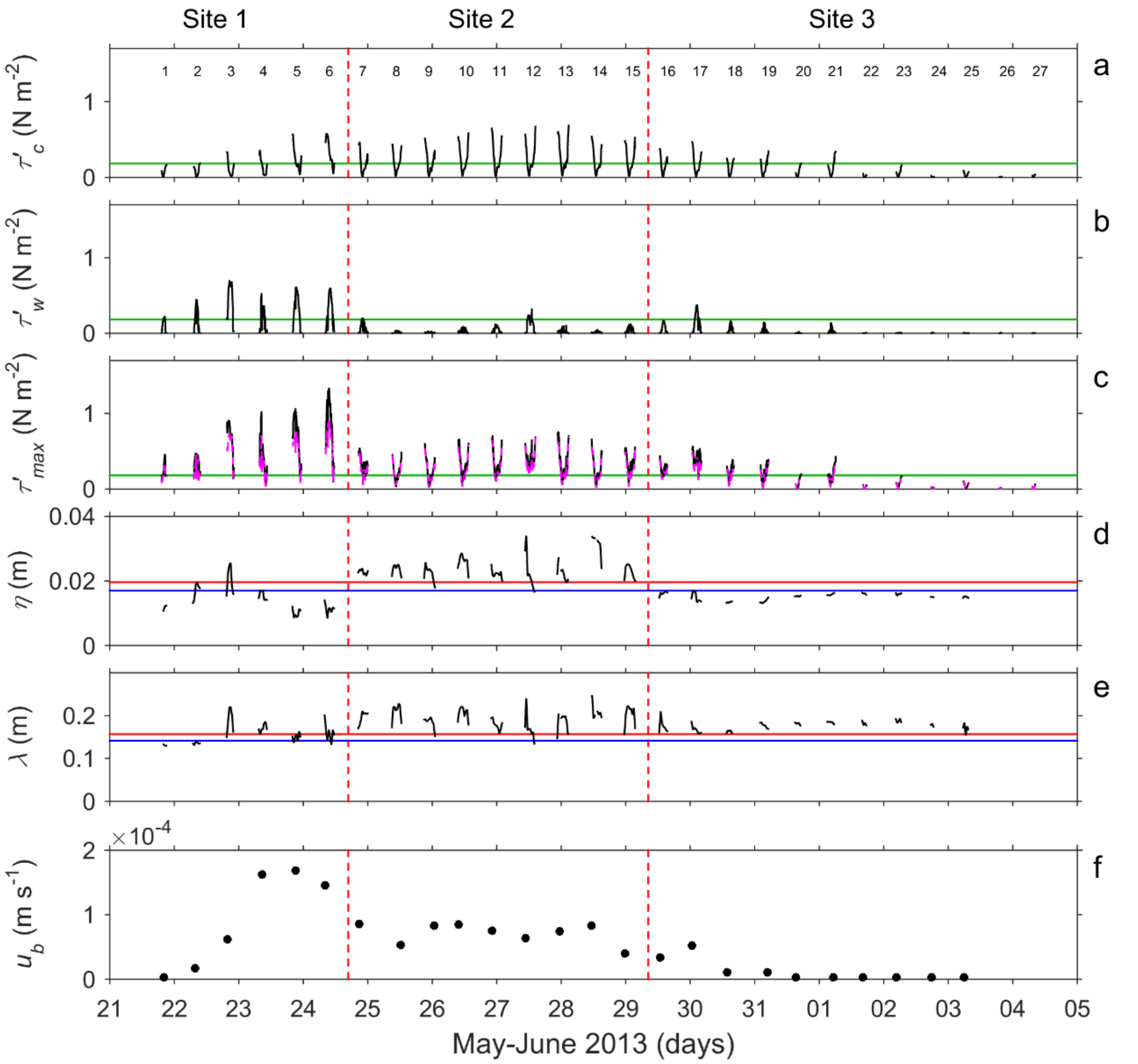

Figure 7: Times series of (a) current-only bed shear stress, τ'_c; (b) wave-only bed shear stress, τ'_w; (c) combined maximum bed shear stress, τ'_{max} and linear maximum bed shear stress, τ'_{maxl} (magenta dashed line); (d) bedform height, η; (e) bedform length, λ; and (f) maximum bedform migration rate, u_b, for each tidal cycle derived from the 3D-ARP scans (the rest of the data have been omitted to highlight the overall trend in the record). The vertical red dashed lines mark the times when the instruments were moved between sites. The horizontal green lines denote the critical stress limit of sediment motion from Soulsby and Whitehouse's equation (Soulsby, 1997), for D_{50} = 227 µm, 0.18 N m^{-2}. In d and e, the blue and red lines are the equilibrium ripple dimensions of Baas (1999) and Soulsby *et al.* (2012), respectively. The data shown are for when the tidal flats were inundated with water above the height of the sensors, processed for a 30-minute window. The numbers in (a) denote the tidal periods for reference.

4.3. Bedform types and migration

The seabed was covered by two-dimensional and three-dimensional bedforms. Two-dimensional bedforms evolved into three-dimensional bedforms on the evening of 22 May at Site 1 and persisted at Site 2 (Figure 8c). The three-dimensional bedforms were replaced by two-dimensional bedforms on 30 May at Site 3 (Figure 8d). Two characteristic 3D-ARP scans, 30 minutes apart from Site 1 (Figure 8a and b) exhibit two-dimensional bedforms with distinct bifurcations, thus suggesting a significant wave influence (Allen, 1968). Examples of the three-dimensional bedforms from Site 2 and the two-dimensional bedforms with sinuous crest lines from Site 3 are shown in Figures 8c and 8d, respectively. The time-series of mean bedform height and length for each 3D-ARP scan are plotted in Figures 7d and 7e. The predicted equilibrium heights and lengths for current ripples of 0.017 m and 0.141 m (Baas, 1999) and from equation 9 of 0.020 m and 0.157 m (Soulsby *et al.*, 2012) are shown for comparison. At Sites 1 and 3, the measured bedform heights were similar to these predicted equilibrium bedform heights. However, there is some indication that the height of the bedforms scaled with the wave forcing at Site 1, as expected for wave ripples (Soulsby, 1997). A period of strong wind-driven currents and wave forcing at Site 1 lead to a decrease in bedform height, *e.g.* on 24 May (Figure 7d). At Site 2, the bedforms were consistently higher than the predicted equilibrium height for current ripples, suggesting that during high tidal currents the bedforms resided within the stability regime of the ripple-dune transition (*cf.* Bennett and Best, 1996; Baas 1999), where the height of the bedforms scales with the water depth and the bed shear stress (van Rijn, 1984; van den Berg and van Gelder, 1993; Soulsby 1997). In summary, the bedforms that developed at Site 1 were wave-influenced current ripples, Site 2 was dominated by transitional bedforms between ripples and dunes, while current ripples close to equilibrium dimensions prevailed at Site 3 (Figure 7d and e).

A time-series of maximum bedform migration rate for each tidal cycle was derived from the 3D-ARP scans (Figure 7f). The migration rates at Site 1 appear to have been enhanced by wind-driven flow and waves. The bedforms at Site 2, which was sampled during a period of relatively fast-flowing tidal currents, had higher migration rates than the bedforms at Site 3, where bed shear stresses were only able to move the bedforms during the last two days in May. It appears that the bedforms stopped migrating on 31 May at Site 3.

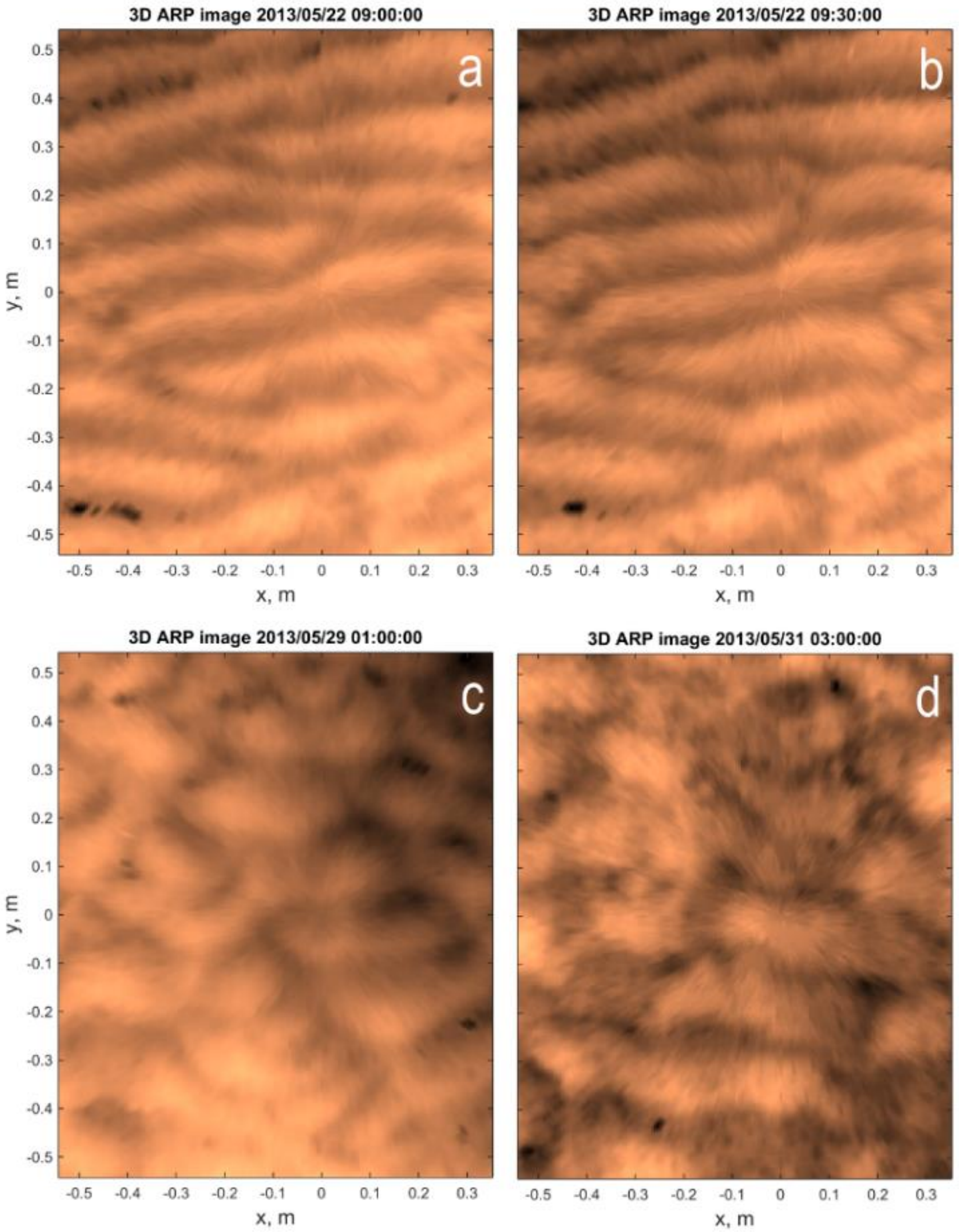

Figure 8: (a, b) A pair of 3D Acoustic Ripple Profiler (3D-ARP) scans from Site 1. The spatially averaged migration distance, determined by 2D cross-correlation, and migration rate were 0.015 m and 8.33×10^{-6} m s^{-1}, respectively. (c) A 3D-ARP scan from Site 2 showing short-crested, three-dimensional bedforms. (d) A 3D-ARP scan from Site 3 showing two-dimensional sinuous bedforms.

4.4. Comparing flow forcing and ripple migration

The relationship between bedform migration rate, u_b, and skin friction Shields parameter, $\theta'_{\max}$, for the tidal flats in the Dee estuary is shown in Figure 9. The bedform migration rate was assumed to be in the same direction as the maximum shear stress, without any lag in the response to changes in $\theta'_{\max}$. The 95% confidence interval of the migration rate is in the range 5.11×10^{-7} to 1.41×10^{-6}, shown by the error bars on the markers in Figure 9. The regression fit line for the laboratory-derived data of Baas *et al.* (2000) is shown for comparison, as the black line in Figure 9. The field data reveal a strong positive correlation between u_b and $\theta'_{\max}$. This relationship can be described by a power function, as for equation 2 from Baas *et al.* (2000), with $R^2 = 0.89$ based on an orthogonal least squares regression with $\alpha = 0.2014$ m s^{-1} and $\beta = 4.23$, shown as a solid grey line in Figure 9. The data along the line of 'no migration', shown as dashed horizontal grey line in Figure 9, were excluded from the regression analysis, as these data are at or below the resolution limit of the 3D-ARP and it was unclear whether these bedforms moved very slowly or were stationary. Based on Soulsby and Whitehouse's formula for the critical Shield parameter of motion (Soulsby, 1997), sediment motion in 227 μm sand is expected for $\theta' > 0.051$. The no migration points, seen in Figure 9 for stresses much higher than this critical threshold, correspond to high wave stress combined with very low current stress, or high bed cohesive clay and EPS content. These high cohesive clay fractions were present at Site 3, as can be seen in Figure 4, where the bed shear stresses were small compared to the other two sites, shown in Figure 7c. The mobile bedforms with low cohesive clay content, which dominated during the sampling of Sites 1 and 2, scatter round the regression fit line of $\theta'_{\max}$ and u_b in Figure 9. The majority of migration rates for the mixed-sediment bedforms in the field were lower than the migration rates of the pure-sand bedforms from the laboratory in Figure 9 (*cf*. filled circles, ●, with black line).

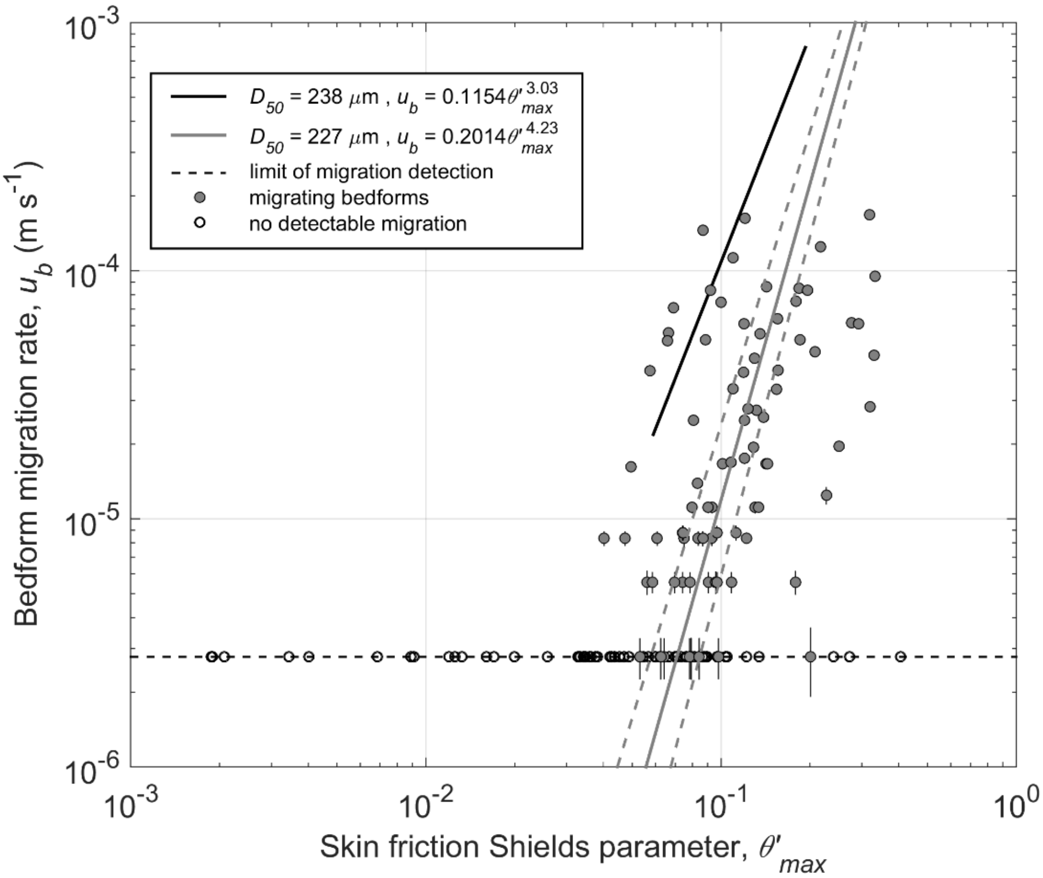

Figure 9: Bedform migration rate against skin friction Shields parameter for combined currents and waves. The black line denotes the 238 µm regression fit for the clean sand laboratory data of Baas *et al.* (2000), as in Figure 1. The dashed black horizontal line and the superimposed open circles denote the lowest measurable migration rates by the 3D-ARP. These data were excluded from the regression analysis. Two extreme values greater than 2.58 standard deviations (outside 99% of the data) were also excluded from the regression analysis. The remaining values were used in the regression fit (n = 81). The regression fit equation for the field data is represented by the solid dark grey line, and the dashed dark grey lines denote the 95% confidence limits of the regression fit line. The error bars for u_b represent the 95% confidence limits of the migration points.

4.5. Bed material transport rate

The scatter in the migration rates for the field data (Figure 9), and the fact that most of these rates are lower than the pure-sand migration rates, suggests that in addition to the maximum skin friction bed shear stress, the difference in bed cohesive clay content also has an effect on the migration rates. The bed material transport rate, Q_b (calculated from equation 4), depends on the bedform migration rate, u_b, but u_b also depends on the bed shear stress and can be affected by the bed cohesive clay content. Hence, α and β in equation 2, and in its equivalent for Q_b, should depend on the cohesive clay present in the bed. In order to investigate this dependence, a subset of the data, where bedform migration occurred, was extracted from the beginning and end of each tidal inundation (Figures 6 and 7), hence temporally closest to the cohesive clay contents from the bed samples collected between inundations. With the exception of Site 1, this corresponds to minimal enhancement of the maximum shear stress by waves.

It is interesting to note that the cohesive clay content in these bed samples correlates well with the duration of each of the 27 inundations over the spring-neap cycle (Figure 10a) ($R^2 = 0.82$, $p < 0.05$ and RMS error = 0.52, for $n = 27$). The bed cohesive clay content is the result of the availability of cohesive clay in the local sediment system and of the processes that affect the cohesive clay mixing into and winnowing from the bed. These processes are influenced by many factors including: bed shear stress and the duration of applied stress; bedform transport rate; D_{50} of the sand component; clay and biological cohesive strength; filtering, excretion and bed re-working by biological organisms; and consolidation during tidal flat exposure (Winterwerp and van Kesteren, 2004). As the bed cohesive clay content is the result of these factors but can also influence many of these factors, the interaction between them needs to be considered as part of a model of bed material transport. The duration of tidal inundation on the flats can encompass a number of these factors as it is controlled by the spring-neap tidal cycle and relates to the maximum stress of the tide, duration of stress, and duration of consolidation. This relationship is specific to these particular field conditions, but helps to emphasize the consistency of this subset of the field data. However, using the duration of tidal inundation in a regression model would restrict the application of the results to tidal flats.

Added to the extracted subset of the field data are the clean sand data (D_{50} = 238 μm) from the laboratory-based migration data of Baas *et al.* (2000) (Figure 1), to provide values for sediment without cohesive clay, since all the field sediment samples contained at least some cohesive clay. There is a statistically significant inverse linear relationship between bed material transport rate and bed cohesive clay content for this composite dataset (Figure 10b; $R^2 = 0.44$, $p < 0.05$ and RMS error = 0.46, for $n = 41$). Baas *et al.* (2013) found a similar inverse relationship between bed material transport rate and kaolin clay content in laboratory experiments. However, there is far greater scatter in the present case because of the additional dependence on shear stress and because these data are from natural sites with other influencing factors ($0.06 < \theta'_{max} < 0.2$ for the lab and $0.05 < \theta'_{max} < 0.4$ for the field).

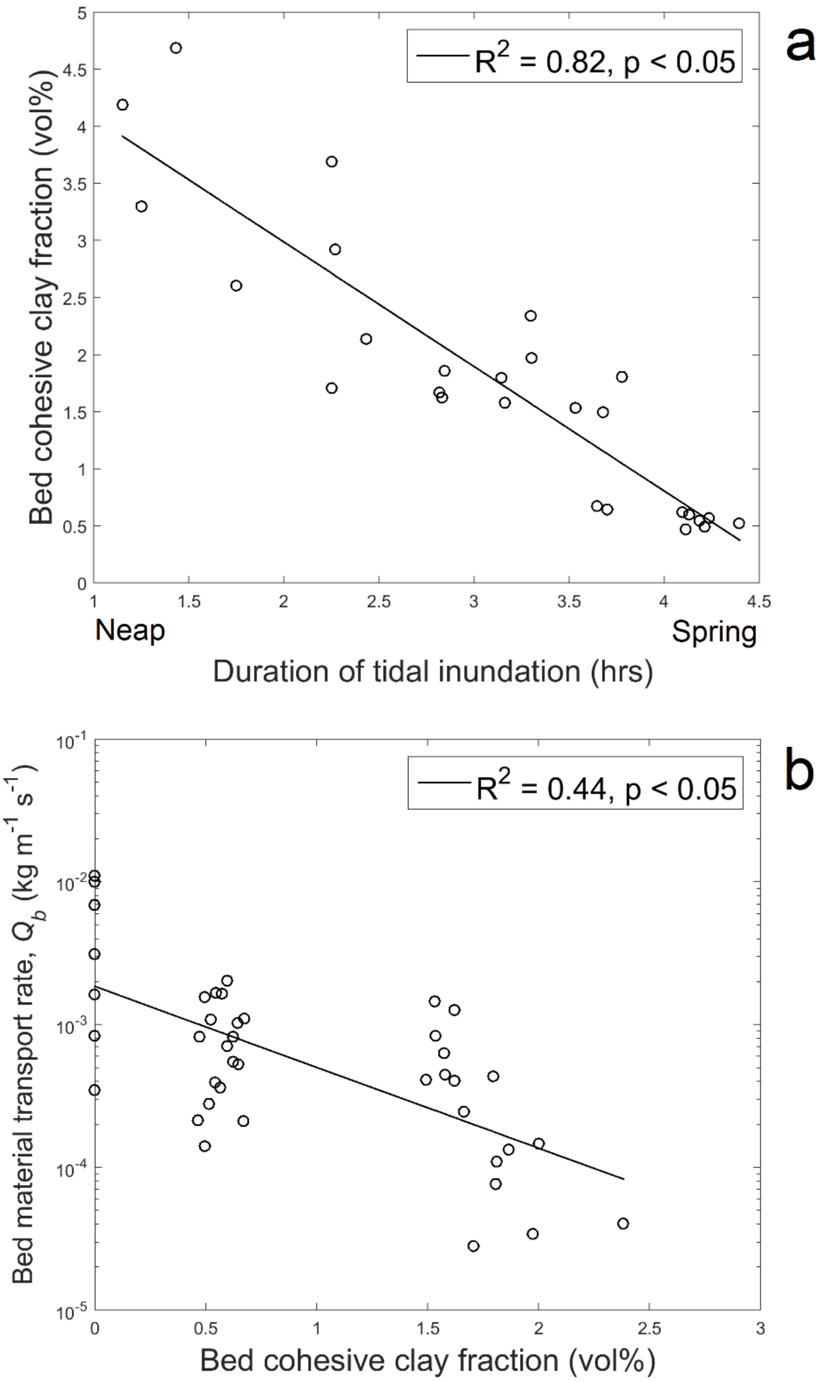

Figure 10: (a) Relationship between duration of tidal inundation, in hours, and bed cohesive clay content for each tidal inundation period (n = 27). (b) Relationship between bed material transport rate and bed cohesive clay fraction (maximum flood and ebb values for each tidal inundation period, n = 41). The data for clay-free sand (D_{50} = 238 μm) from Baas *et al.* (2000) are also included for zero cohesive clay values.

In equation 2, the nature of the dependence of α and β on the bed cohesive clay content can be explored by using a multiple linear regression (Kennedy and Neville, 1976; Chatterjee and Hadi, 2015), for which the laboratory data of Baas *et al.* (2000) provides values for zero cohesive clay. After performing ordinary least squares multiple linear regression, a two-sample F-test demonstrated that the laboratory data of Baas *et al.* (2000) have a significantly lower error variance than the field data, probably because these data were collected under controlled laboratory conditions. A robust multiple linear regression method, in the form of an iteratively re-weighted least squares method, was used to control for the differences in variance of the combined data set (Wilcox, 2012; Chatterjee and Hadi, 2015). The initial weights for this regression method were estimated from the inverse of the variance of the errors of the field and laboratory data, determined by ordinary least squares regression (Wilcox, 2012; Chatterjee and Hadi, 2015). This robust regression also reduces the effect of extreme outliers as part of the iterative re-weighting process. The inclusion of the laboratory data forced the fit to zero cohesive clay values. A limit of 0.05 significance was chosen for the multiple linear regression model. Overall, the model was significant, with an $R^2 = 0.993$, $p < 0.05$ and RMS error = 0.33, for $n = 41$ (Table 3; Kennedy and Neville (1976)), and yielded the following equation:

$$Q_b = 10^{0.13-1.70c} \times (\theta'_{\max})^{2.98-1.06c}$$

$$\text{for } 0 \leq c < 2.8 \text{ vol\%} \quad , \quad \theta'_{\max} > 0.051 \qquad (11)$$

where Q_b is the mass transport rate (kg m^{-1} s^{-1}), $\theta'_{\max}$ is the skin-friction related Shields parameter, and c is the bed cohesive clay content (vol%). The power coefficient of $\theta'_{\max}$ in equation 11 at 0 vol% cohesive clay, 2.98, is close to 3.03, the power coefficient for 238 μm sand, showing that equation 11 reduces close to the slope of the equation of Baas *et al.* (2000; Figure 1) for zero bed cohesive clay content. Equation 11 predicts a very small, constant bed material transport rate ($Q_b = 2.24\times10^{-5}$ kg m^{-1}s^{-1}) for a bed cohesive clay content equal to 2.8

vol%. c = 2.8 vol% corresponds to a bed EPS content of 0.06 wt% for equation 10, which is close to the 0.063 wt% limit for bedform migration/development of Malarkey *et al.* (2015). The relative importance of the parameters in equation 11 can be determined by dividing the coefficients by their standard errors (t statistic in Table 3) and comparing the magnitude of the values (Borradaile, 2003). The maximum skin-friction related Shields parameter has the highest value, 55.7, and the greatest relative influence on the bed transport (52%), followed by the cohesive clay content, 30.2 (28%). The interaction between Shields stress and cohesive clay has a value of 17.7 (17%) and has the third greatest influence on the bed transport (Table 3).

Table 3: Multiple linear regression statistics for bed material transport analysis

$\log_{10}(Q_b) = a_1 + a_2 \times c + a_3 \times \log_{10}(\theta'_{max}) + a_4 \times c \times \log_{10}(\theta'_{max})$

	Coefficient	Standard Error	t Statistic	*p-value*	*% influence*
a_1 (intercept)	0.13	0.050	2.654	1.165×10^{-2}	2.5
a_2 (c)	-1.70	0.056	-30.160	1.190×10^{-27}	28.4
a_3 (θ'_{max})	2.98	0.054	55.658	2.812×10^{-37}	52.4
a_4 (c×θ'_{max})	-1.06	0.060	-17.683	1.235×10^{-19}	16.7

Number of observations: 41, Error degrees of freedom: 37

RMS Error: 0.327, R^2: 0.993

F-statistic vs. constant model: 1.83×10^3, p for model overall = 2.86×10^{-40}

Equation 11 is plotted for set values of bed cohesive clay content (0 to 2.5 %) in Figure 11. The line of ‘no motion’ corresponds to 2.8 %, which is the effective limit of detection of bed material transport, with an equivalent bedform height of 0.008 m (minimum estimated height from the observed bedforms) associated with the minimum migration rate. Figure 11 shows that a higher bed shear stress is required to produce a given bed material transport rate, as bed cohesive clay content increases. In the discussion section, the scatter of the data in relation to the lines derived from equation 11, seen in Figure 11, is considered further.

Equation (11) was defined for $\theta > \theta_{cr}$ (θ_{cr} = 0.051). However, if the lines in Fig. 11 are extrapolated back to the minimum measurable transport rate ($Q_{b0} = 2.24\times10^{-5}$ kg m^{-1}s^{-1}) then there is a common value of θ, θ_c, where all lines intersect, θ_c = 0.025 which is about half the Soulsby (1997) value of 0.051 for the D_{50} of the sediment. This is a reasonable value bearing in mind the typical scatter about Shields curves for flat beds and the fact that local shear-stress enhancement at the ripple crest can still result in slow migration below the flat-bed threshold. If bed material transport rate is defined as the excess above Q_{b0} as has been done for flat beds (Shvidchenko et al., 2001) then the transport rate can include this threshold

$$Q_b - Q_{b0} = 10^{0.13-1.70c}(\theta'_{\max} - \theta_c)^{2.98-1.06c}, \quad \theta'_{\max} \geq \theta_c,$$

where θ_c = 0.025. The fact that this threshold stress does not depend on clay content, c, (unlike for example Jacobs et al., 2011) is justifiable because of the modest clay content range involved ($0 \leq c \leq 2.8\%$).

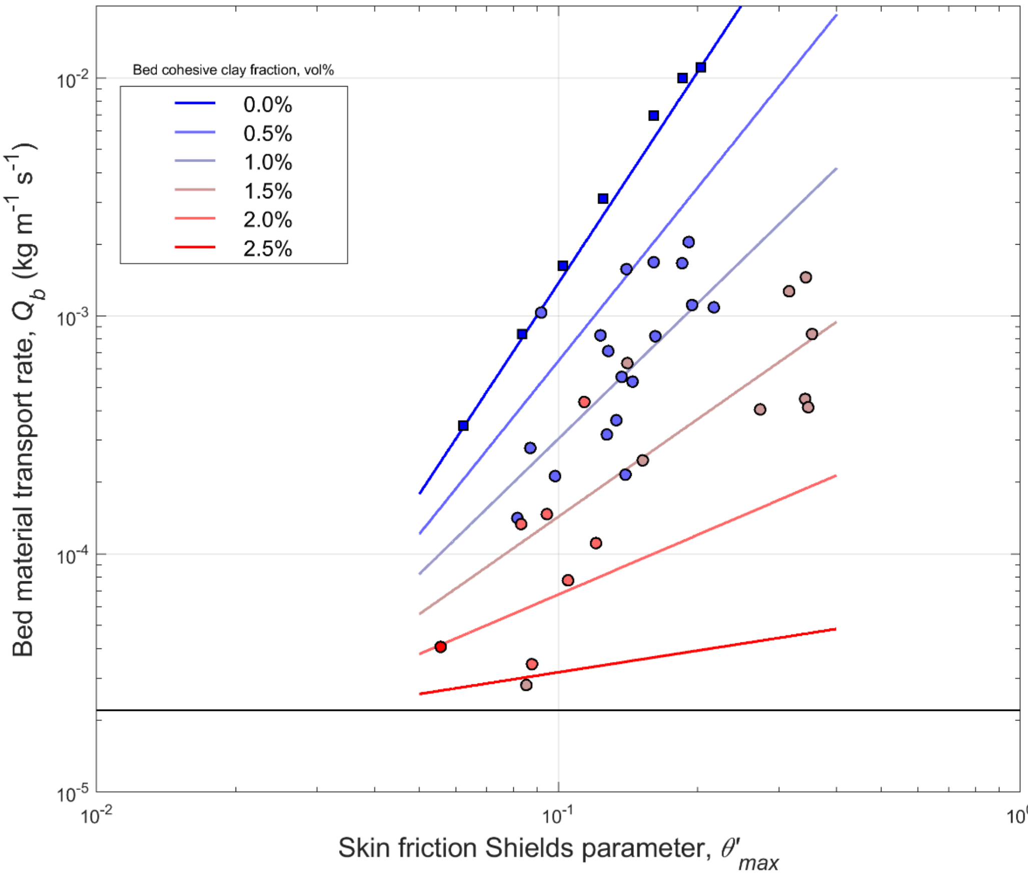

Figure 11: Maximum bed material transport rate, for flood and ebb, against skin friction Shields parameter for combined currents and waves. The color-filled circles denote the measured data, where the colors represent the bed cohesive clay fraction binned in 0.5 vol% intervals. The black horizontal line represents the minimum bed material transport rate, based on the lowest measurable migration rate by the 3D-ARP and a 0.008 m high bedform (or *c* = 2.8 vol% in equation 11) and can be treated as the line of no motion. The colored lines denote the multiple linear regression fit, equation 11, calculated for set bed cohesive clay content values. The data for clay-free sand (D_{50} = 238 µm) from Baas *et al.* (2000) were included in regression analysis, forcing the fit to these zero cohesive clay fractions (square markers).

5. Discussion

5.1. Comparing the laboratory and field data

Bedform migration rates in the field were lower than in the experiments of Baas *et al.* (2000) (Figure 9), at times when the bed cohesive clay content in the field was below about 2.5 vol%. At higher cohesive clay contents, which coincided with high EPS contents and were most common at Site 3, bedform migration and bed material transport was not detectable in the study area (Figures 7f, 9 and 11). The lack of mobility of the sediment from 31 May onward at Site 3 cannot be explained solely by the relatively weak neap tides (*cf.* Figure 7c and f), because there were periods when the bedforms did not migrate even though the bed shear stress was above the expected threshold of sediment movement, *i.e.*, $\tau'_{max} > 0.18$ N m^{-2} for $D_{50} = 227$ μm (Soulsby, 1997).

The multiple regression analysis shows that the bed cohesive clay content, in conjunction with bed shear stress, had a large influence on the bed material transport rate. The clay minerals and the EPS matrix are inferred to have formed cohesive bonds between the sand particles, which: (1) increased the bed shear stress required for bed material transport; (2) progressively reduced the bed material transport rate as the bed cohesive clay content increased from 0 vol% to 2.8 vol%; and (3) halted detectable bedform migration and bed material transport at the field sites at bed cohesive clay contents above about 2.8 vol% and bed EPS contents above about 0.05 wt%. This value of 2.8 vol% cohesive clay is remarkably low, and well within the 'clean sand' category of Shepard (1954) and the 'mature sand' (arenite) category of Dott (1964). Although a direct comparison with the mixed mud-sand experiments of Baas *et al.* (2013) is not possible, because the sand size, clay type and flow conditions differed from those at the field sites, it is notable that the bed material transport rates in these experiments were significantly reduced at low bed clay fractions of < 2% (Baas *et al.*, 2013).

The positive correlation between bed cohesive clay and EPS fractions (Figure 5), given by equation 10, may explain the large difference between sediment mobility at Sites 1 and 2 compared to Site 3. The bed sampled towards the end of the SEDbed deployment at Site 3 were sufficiently cohesive (biologically and physically) to reduce the migration of bedforms below the limit of detection, whereas bedform development and migration occurred throughout data collection at Sites 1 and 2, because biological and physical cohesion were weak enough to allow sediment movement. Malarkey *et al.* (2015) found that the rate of bedform development was substantially reduced on a flat sand bed that contained more than 0.063 wt% EPS. Using the laboratory experiments of Malarkey *et al.* (2015) as a guide, the EPS fractions of 0.02-0.04 wt% for Sites 1 and 2 may therefore have been too low to significantly hinder bed sediment movement and bedform development, whereas the EPS fractions of 0.08-0.21 wt% for Site 3 may have been too high for bedform development (Figure 5).

The linear relationship between bed cohesive clay content and bed EPS content in equation 10, may support the alternate states model of van de Koppel *et al.* (2001), see also Friend *et al.* (2008), which advocates that a sediment bed tends to switch between two stable states: low concentrations of diatoms (main EPS producers) and high bed shear stress, as for Sites 1 and 2, versus high concentrations of diatoms and low bed shear stress, as for Site 3. The bed would have been in an unstable state between these limits, if the model of van de Koppel *et al.* (2001) applies to the studied sites in the Dee estuary. Specifically, the bed cohesive clay content increased as the hydrodynamic forcing decreased at Site 3 and the bedform migration reduced as a result of the increased bed cohesive clay content. This implies that the behavior of the bed changed from being dominated by non-cohesive processes to being dominated by cohesive processes over the spring-neap cycle, a transition that could be enhanced by the production of EPS (van de Koppel *et al.*, 2001). For the energetic conditions at Sites 1 and 2, caused by strong wave action and high maximum current velocities during spring tides, non-cohesive sediments prevailed, allowing bedforms to form and migrate much more easily than for the calmer conditions at Site 3 (*cf.* Figures 6a to 6c, 6f and 10).

5.2. Duration of tidal inundation and bed cohesive clay content

Long periods of tidal inundation (i.e. at spring tide) may carry greater amounts of sediment and allow more time for settling to occur than short periods, leading to increased deposition (Friedrichs, 2011; Kirwan and Guntenspergen, 2012). However, this increased deposition relies on a flood-ebb asymmetry in the tide and little wave forcing, or the reduction in stress by salt marsh plants, to promote deposition and prevent the erosion of newly deposited sediment (Friedrichs, 2011; Fagherazzi, 2012). In Figure 10a the opposite trend is apparent, with bed cohesive clay content reducing with increasing duration of tidal inundation.

As the tidal inundation period decreases, the period of bed strengthening due to atmospheric exposure increases, making the bed more resistant to erosion (Amos *et al.*, 1988; Whitehouse *et al.*, 2000). At spring tide, the bed has less time to consolidate, so the deposited material is more easily removed with the next flood tide. At neap tide, the bed strengthening time is longer and deposited material is more resistant to erosion on the flood. High bed shear stress during spring tide can prevent the permanent deposition of clay and increases winnowing. Although increasing flow velocity increases the particle encounter rate for filter feeders, it can also reduce filtering efficiency resulting in less sediment being removed from suspension to the bed (Shimeta and Jumars, 1991). Reduced flow velocity at neap tide will allow the deposition of clay, with cohesion preventing re-suspension on the ebb, in addition to biological filtering and excretion. Further to this, biological mixing will work the clay into the bed (Passarelli *et al*, 2014). These mechanisms are proposed as an explanation for the inverse relationship between duration of tidal inundation and bed cohesive clay content.

5.3. Limitations

The scatter in the field data presented in Figure 9 was greater than for the laboratory results, despite the strong correlation between ripple migration rate and skin friction Shields parameter for the field data and the similar behavior between the field and laboratory for cohesive clay and EPS fractions below 2.8 vol% and 0.05 wt%, respectively. This probably reflects the fact that field conditions are inherently more complex, and therefore more variable than laboratory conditions. The main sources of this data scatter are outlined below.

The dynamics of the bedforms in the Dee Estuary depended on the combined action of waves and current, whereas the bedforms in the laboratory formed in steady, uniform flow. Waves enhance sediment transport when they coincide with currents (Grant and Madsen, 1979; Pattiaratchi and Collins, 1984). This promoted bedform migration for the wave influenced Site 1 (Figure 7f) in comparison to the other sites and the laboratory experiments of Baas *et al.* (2000), where the waves were much smaller and absent, respectively. This wave enhancement also explains the small amounts of mud at Site 1 compared to Site 3, due to the greater effect of winnowing of fine sediment and EPS by waves at Site 1 (Baas *et al.*, 2014).

The laboratory ripples of Baas *et al.* (2000) were given enough time to attain equilibrium size in steady, uniform flows, before migration rates were measured. In contrast, the bedforms in the Dee Estuary were probably not in equilibrium with the changing tidal flows, wave forcing, water levels and sediment cohesive properties. It is more likely that most of these bedforms were continually adapting to changes in the hydrodynamic forcing. Non-equilibrium current ripples have been shown to migrate faster than equilibrium ripples (Baas, 1999). Non-equilibrium dunes, on the other hand can move faster or slower than equilibrium dunes, depending on whether the non-equilibrium dunes evolve to a smaller or larger equilibrium size (Allen, 1984). This so-called bedform hysteresis may have introduced scatter in the relationship between the instantaneous flow forcing and bedform migration rate (Figure 9) and therefore bed material transport rate (Figure 11).

Other possible sources of the data scatter include: (1) uncertainties in calculating the non-linear effect of wave forcing on bed shear stress (Malarkey and Davies, 2012); (2) the effects of non-translational changes in plan morphology of the rippled beds, caused by, for example, bedform hysteresis and flow rotation, on the 2D cross-correlation procedure used to calculate bedform migration rate from the 3D-ARP scans; (3) spatial and temporal variations in the clay-mud ratio used to convert bed mud fractions into cohesive clay fractions; (4) uncertainties in the bedform shape factor, bed porosity, and sediment loss-gain factor used to calculate the bed material transport rate in Equation 4; and (5) variation in biogenic effects such as biostabilization and bioturbation (Black *et al*, 2002).

5.4. Implications for sediment transport modelling, geomorphology, and coastal engineering

Despite the above limitations, it has been shown that the bed material transport rates for the biologically active mixed sand-mud under field conditions in the Dee Estuary were significantly reduced for bed cohesive clay fractions below 2.8 vol% and for EPS fractions below 0.05 wt%, due to physical and biological cohesion. This is below the 3-5% clay content found for the transition to a cohesion-dominated eroding bed (van Ledden *et al.*, 2004), but above the EPS fraction (0.026%) found to stabilize wave ripples by Friend *et al.* (2008). These results have important implications for sediment transport modelling. Since the bed material transport rate depends on the strength of biological and physical cohesion, clean sand formulae should only be used if bed cohesive clay and EPS contents are close to zero. In addition, bed material transport reduced below the limit of detection, of the 3D-ARP, for bed cohesive clay content above about 2.8 vol%, in the present study. Equation 11 can be used to estimate bed material transport rates for different bed cohesive clay contents below 2.8 vol%. The implications of this work for sediment transport modelling also extend to larger-scale geomorphology and coastal engineering. For example, slowing down bedform migration at the unexpectedly low bed mud contents found in this study may add to the stability of nearshore environments and therefore influence shoreline change, longshore sediment transport, intertidal channel switching, and other nearshore processes.

6. Conclusions

A comparative analysis of bedform migration and sediment transport in a biologically active mixed sand-mud environment in the Dee Estuary, northwest UK, under the influence of currents and waves, and sand-only steady-current laboratory experiments was conducted. The sediment bed at the field sites changed rapidly from weakly cohesive (below 2 vol% cohesive clay) to strongly cohesive (up to 5.4 vol% cohesive clay), as the tide progressed from spring towards neap, and wave forcing decreased. The reduction in forcing allows clay to settle out of the water column and also be worked into the bed by various physical and biological processes. This general trend can be seen in the inverse relationship between the duration of tidal inundation and clay content shown in Figure 10a, where the duration of tidal inundation is a proxy for flow strength. The concentration of biological cohesive material (EPS) in the bed sediment correlated linearly with the cohesive clay content.

The results demonstrate that, once the effect of waves had been accounted for, the bedform migration rate and the bed material transport rate of mixed sediments in the field were significantly different from that of sand-only bedforms even when clay and EPS fractions in the bed were below 2.8 vol% and 0.05 wt%, respectively. Below these limits the bed material transport rate reduced as the bed cohesive clay and EPS content increased (Figure 11). Above these limits, which correspond approximately to the points where clay and EPS began to significantly affect the migration rate in the mixed clay-sand laboratory experiments of Baas *et al.* (2013) and the mixed sand-EPS laboratory experiments of Malarkey *et al.* (2015), bedform migration and bed material transport were below measureable limits in the study area. Presumably, the cohesive bonding of sand particles by clay and EPS was sufficiently strong to resist the boundary shear stress from currents and waves above 2.8 vol% cohesive clay and 0.05 wt% EPS.

These results have important practical implications for the wider prediction of sediment transport in models, since existing formulae for the transport rate associated with bedform migration should only be applied when cohesive clay and EPS content is close to zero. On a broader scale, the management of coastal morphological change, the assessment of the environmental impact of dredging operations in estuaries, and the understanding of the effects of climate-induced habitat change in shallow-marine environments are expected to benefit from the present study, by means of improved predictions of bed material transport.

Acknowledgements

This work was supported by the UK Natural Environment Research Council (NERC) under grant NE/I027223/1 (COHBED), by core funding from NERC to the National Oceanography Centre, and by a NERC PhD studentship to the first author. We are grateful to the NOC Ocean Technology and Engineering group for instrument set up and deployment, and to the Liverpool Bay Coastal Observatory for the weather data. Algorithms for the 3D-ARP processing and the PUV method were written by Paul Bell and Judith Wolf, respectively. Paul Bell also kindly provided the Radon transform method for correcting the bedform orientations. David Paterson received funding from the Marine Alliance for Science and Technology for Scotland (MASTS), funded by the Scottish Funding Council (grant reference HR09011) and contributing institutions. Andrew Manning's contribution to this manuscript was partly funded by HR Wallingford Company Research project 'FineScale - Dynamics of Fine-grained Cohesive

Sediments at Varying Spatial and Temporal Scales' (DDY0523). We would also like to thank Robert Lafite, Martin Austin and the anonymous reviewers for their comments on this manuscript.

The authors have no conflicts of interest regarding this work.

Data availability

All data are available upon request to the authors and are banked at the British Oceanographic Data Centre (http://www.bodc.ac.uk/).

References

Aldridge, J. N., E. R. Parker, L. M. Bricheno, S. L. Green, and J. van der Molen (2015), Assessment of the physical disturbance of the northern European Continental shelf seabed by waves and currents, *Continental Shelf Research*, 108, 121-140, doi: 10.1016/j.csr.2015.03.004.

Allen, J. R. L. (1968), *Current Ripples: Their relation to patterns of water and sediment motion*, North-Holland Publishing Company, Amsterdam.

Allen, J. R. L. (1984), *Sedimentary Structures: Their character and physical basis*, Elsevier, Amsterdam.

Amos, C.L., N. A., Van Wagoner, and G. R., Daborn, (1988), The influence of subaerial exposure on the bulk properties of fine-grained intertidal sediment from Minas Basin, Bay of Fundy. *Estuarine, Coastal and Shelf Science*, 27, 1-13.

Amoudry, L. O., Bell, P. S., Black, K. S., Gatliff, R. W., Helsby, R., Souza, A. J., Thorne, P. D., Wolf, J. (2009), A Scoping Study on: Research into Changes in Sediment Dynamics Linked to Marine Renewable Energy Installations. [pdf] Available at: https://tethys.pnnl.gov/sites/default/files/publications/Amoudry_2009.pdf [Accessed 23 July 2014], p. 120.

Amoudry, L. O., and A. J. Souza (2011), Deterministic coastal morphological and sediment transport modelling: a review and discussion, *Reviews of Geophysics*, 49, 1-21.

Baas, J. H. (1999), An empirical model for the development and equilibrium morphology of current ripples in fine sand, *Sedimentology*, 46, 123–138.

Baas, J. H., R. L. van Dam, and J. E. A. Storms (2000), Duration of deposition from decelerating high-density turbidity currents, *Sedimentary Geology*, 136, 71-88.

Baas, J. H., J. L. Best, and J. Peakall (2011), Depositional processes, bedform development and hybrid bed formation in rapidly decelerated cohesive (mud-sand) sediment flows, *Sedimentology*, 58, 1953-1987, doi: 10.1111/j.1365-3091.2011.01247.x.

Baas, J. H., A. G. Davies, and J. Malarkey (2013), Bedform development in mixed sand-mud: The contrasting role of cohesive forces in flow and bed, *Geomorphology*, 182, 19-39.

Baas, J. H., A. Westlake, J. Eggenhuisen, L. Amoudry, M. Cartigny, N. Coultish, S. McLelland, D. Mouazé, B. Murphy, D. Parsons, K. Rosewell, G. Ruessink, R. Schrijvershof, X. Wu, and L. Ye (2014), Wave ripples in mixtures of cohesive clay and cohesionless sand: Preliminary results, in *Proceedings of the HYDRALAB IV Joint User Meeting, Lisbon, July 2014*, 1-9.

Bell, P. S., and P. D. Thorne (1997), Application of a high resolution acoustic scanning system for imaging sea bed microtopography, in *7^{th} International Conference on Electronic Engineering in Oceanography – Technology transfer from research to industry, IEEE conference Publication no.* 439, 128-133.

Bendat, J. S., and A. G. Piersol (1986), *Random Data: Analysis and Measurement Procedures*, 2^{nd} edition, John Wiley & Sons, New York.

Bennett, S. and J. Best, (1996), Mean flow and turbulence structure over fixed ripples and the ripple-dune transition. In: P. J. Ashworth, S. J. Bennett, J. L. Best, and S. J. McLelland eds. 1996. *Coherent Flow Structures in Open Channels*. Hoboken, N. J.: John Wiley. 67– 125.

Black, K. S., T. J., Tolhurst, D. M. Paterson, and S. E. Hagerthey, (2002), Working with natural cohesive sediments, *Journal of Hydraulic Engineering*, 128 (1), 1-7.

Bolaños, R., P. D. Thorne, and J. Wolf (2012), Comparison of measurements and models of bed stress, bedforms and suspended sediments under combined waves, *Coastal Engineering*, 62, 19-30.

Borradaile, G. J. (2003), *Statistics of Earth Science Data: Their Distribution in Time, Space and Orientation*, Springer-Verlag, Berlin.

Brown, J. M. (2010), A case study of combined wave and water levels under storm conditions using WAM and SWAN in a shallow water application, *Ocean Modelling*, 35 (3), 215-229, doi: 10.1016/j.ocemod.2010.07.009.

Brown, J. M., and J. Wolf (2009), Coupled wave and surge modelling for the eastern Irish Sea and implications for model wind-stress, *Continental Shelf Research*, 29, 1329-1342.

Chatterjee, S. and A. S. Hadi (2015), *Regression analysis by example*, 5th Ed. Hoboken, Wiley & Sons, New Jersey.

Cowell, P. J., P. S. Roy, and S. A. Jones (1995), Simulation of large-scale coastal change using a morphological behaviour model, *Marine Geology*, 126, 45-61.

Davies, A. G., and P. D. Thorne (2008), Advances in the study of moving sediments and evolving seabeds, *Surveys in Geophysics*, 29 (1), 1-36.

Deacon, G. F. (1894), Discussion on the training of rivers, *Minutes of the Proceedings of the Institute of Civil Engineers*, 118, 93-96.

Dott Jr., R. L. (1964), Wacke, greywacke and matrix – What approach to immature sandstone classification? *Journal of Sedimentary Petrology*, 34, 625-632.

Dubois, M., K. A. Gilles, J. K. Hamilton, P. A. Rebers, and F. Smith (1956), Colorimetric method for determination of sugars and related substances, *Analytical Chemistry*, 28, 350–356.

Fagherazzi, S., M. L. Kirwan, S. M. Mudd, G. R. Guntenspergen, S. Temmerman, A. D’Alpaos, J. van de Koppel, J. M. Rybczyk, E. Reyes, C. Craft, and J. Clough (2012), Numerical models of salt marsh evolution: Ecological, geomorphic, and climatic factors, Reviews of Geophysics, 50, RG1002, doi:10.1029/2011RG000359.

Fenton, J. D., and W. D. McKee (1990), On calculating the lengths of water waves, *Coastal Engineering*, 14, 499-513.

Flemming, B. W. (2002), Geographic distribution of muddy coasts, in *Muddy Coasts of the World: Processes, Deposits and Function*, *Proceedings in Marine Science 4*, edited by T. Healy, Y. Wang and J.-A. Healy, pp. 99–201, Elsevier Science, The Netherlands.

Friedrichs, C.T., 2011. 3.06 - Tidal Flat Morphodynamics: A Synthesis, In: Eric Wolanski and Donald McLusky, Ed. 2011. Treatise on Estuarine and Coastal Science, Waltham: Academic Press, 137-170.

Friend, P. L., C. H. Lucas, P. M. Holligan, and M. B. Collins (2008), Microalgal mediation of ripple mobility, *Geobiology*, 6, 70–82.

Giachetti, A. (2000), Matching techniques to compute image motion, *Image and Vision Computing*, 18, 247–260.

Gordon, L., and A. Lohrmann (2001), Near-shore Doppler current meter wave spectra, in *Ocean Wave Measurement and Analysis: Proceedings of ASCE Waves 2001 conference*, ASCE, Reston, VA.

Grant, J., U. V. Bathmann, and E. L. Mills (1986), The interaction between benthic diatom films and sediment transport, *Estuarine, Coastal and Shelf Science*, 23, 225-238.

Grant, W. D., and O. S. Madsen (1979), Combined wave and current interaction with a rough bottom, *Journal of Geophysical Research*, 84 (C4), 1797-1808.

Hagadorn, J. W., and C. McDowell (2012), Microbial influence on erosion, grain transport and bedform genesis in sandy substrates under unidirectional flow, *Sedimentology*, 59, 795-808.

Halcrow (2013), *North West Estuaries Processes Reports: Dee Estuary*, Sefton Council, Merseyside.

Harris, P. T., E. K. Baker, A. R. Cole, and S. A. Short (1993), A preliminary study of sedimentation in the tidally dominated Fly River delta, Gulf of Papua, *Continental Shelf Research*, 13(4), 441-472.

Hoekstra, P., P. Bell, P. van Santen, N. Roode, F. Levoy, and R. Whitehouse (2004), Bedform migration and bedload transport on an intertidal shoal, *Continental Shelf Research*, 24, 1249-1269.

Hubbell, D. W. (1964), *Apparatus and techniques for measuring bedload*, *U.S. Geol. Survey Water-Supply Paper 1748*, United States Government Printing Office, Washington.

Jacobs, W., P. Le Hir, W. Van Kesteren, and P. Cann (2011), Erosion threshold of sand–mud mixtures, *Continental Shelf Research*, 31(10), 14–25.

Jafari-Khouzani, K., and H. Soltanian-Zadeh (2005), Radon transform orientation estimation for rotation invariant texture analysis, IEEE Transactions on Pattern Analysis and Machine Intelligence, 27 (6), 1004-1008.

Jones, L., A. Garbutt, J. Hansom, and S. Angus (2013), Impacts of climate change on coastal habitats, *MCCIP Science Review 2013*, 167-179, doi:10.14465/2013.arc18.

Kennedy, J. B., and A. M. Neville (1976), *Basic Statistical Methods for Engineers and Scientists*, 2nd Ed., Harper and Row, New York.

Kirwan, M. L. and G. R. Guntenspergen (2012), Feedbacks between inundation, root production, and shoot growth in a rapidly submerging brackish marsh, *Journal of Ecology*, 100, 764-770. doi:10.1111/j.1365-2745.2012.01957.

Lisle, T. E., and S. Hilton (1992), The volume of fine sediment in pools: an index of sediment supply in gravel-bed streams, *Water Resources Bulletin*, 28, 371-383.

Madsen, O. S. (1994), Spectral wave-current bottom boundary layer flows, in *Proceedings of the 24th International Conference on Coastal Engineering, Kobe, Japan*, ICCE (Curran Associates), Red Hook, NY.

Malarkey, J., and A. G. Davies (2012), A simple procedure for calculating the mean and maximum bed stress under wave and current conditions for rough turbulent flow based on Soulsby and Clarke's (2005) method, *Computers & Geosciences*, 43, 101-107.

Malarkey, J., J. H. Baas, J. A. Hope, R. J. Aspden, D. R. Parsons, J. Peakall, D. M. Paterson, R. J. Schindler, L. Ye, I. D. Lichtman, S. J. Bass, A. G. Davies, A. J. Manning, and P. D. Thorne (2015), The pervasive role of biological cohesion in bedform development, *Nature Communications*, 6:6257, doi: 10.1038/ncomms7257.

Manning, A. J., J. V. Baugh, J. R. Spearman, E. L. Pidduck, and R. J. S. Whitehouse (2011), The settling dynamics of flocculating mud-sand mixtures: Part 1 – Empirical algorithm development, *Ocean Dynamics*, 61(2), 311-350, doi: 10.1007/s10236-011-0394-7.

Marine Electronics (2009), User Manual for the 3D Sand Ripple Profiling Logging Sonar, issue 1.1., Marine Electronics Ltd., Vale, Channel Islands, U.K.

Masselink, G., M. J. Austin, T. J. O'Hare, and P. E. Russell (2007), Geometry and dynamics of wave ripples in the nearshore zone of a coarse sandy beach, *Journal of Geophysical Research*, 112, C10022, 1-19.

McDougall, T. J., and P. M. Barker (2011), Getting started with TEOS-10 and the Gibbs Seawater (GSW) Oceanographic Toolbox, SCOR/IAPSO WG127, (http://www.teos-10.org/pubs/Getting_Started.pdf).

Mehta, A. J. (2014), An Introduction to Hydraulics of Fine Sediment Transport. Advanced Series on Ocean Engineering, 38, World Scientific Publishing Company, Singapore, 1039 pp.

Mitchener, H., and H. Torfs (1996), Erosion of mud/sand mixtures. *Coastal Engineering*, 29, 1-25.

Moore, D. M., and R. C. Reynolds, Jr. (1997), *X-Ray Diffraction and the Identification and Analysis of Clay Minerals*. 2nd Edition, Oxford University Press, New York.

Moore, R. D., J. Wolf, A. J. Souza, and S. S. Flint (2009), Morphological evolution of the Dee Estuary, Eastern Irish Sea, UK: A tidal asymmetry approach, *Geomorphology*, 103, 588-596.

Panagiotopoulos, I., G. Voulgaris, and M. B. Collins (1997), The influence of clay on the threshold of movement of fine sandy beds. *Coastal Engineering*, 32, 19-43.

Paphitis, D. (2001), Sediment movement under unidirectional flows: an assessment of empirical threshold curves, *Coastal Engineering*, 43, 227-245.

Parsons, D. R., R. J., Schindler, J. A., Hope, J., Malarkey, J. H., Baas, J., Peakall, A. J., Manning, L., Ye, S., Simmons, D. M., Paterson, R. J., Aspden, S. J., Bass, A. G., Davies, I. D., Lichtman, and P. D., Thorne (2016), The role of biophysical cohesion on subaqueous bed form size. *Geophysical Research Letters*, 43, pp. 1-8, doi:10.1002/2016GL067667.

Passarelli, C., F. Olivier, D.M. Paterson, T. Meziane and C. Hubas (2014), Organisms as cooperative ecosystem engineers in intertidal flats, *Journal of Sea Research*, 92, 92–101.

Paterson, D. M., and K. S. Black (1999), Water flow, sediment dynamics and benthic biology, in advances in ecological research 29, D.B. Nedwell and D.G. Raffaelli, (Eds.), Academic Press, London, UK, 155-193.

Pattiaratchi, C. B., and M. B. Collins (1984), Sediment transport under waves and tidal currents: A case study from the northern Bristol Channel, U.K., *Marine Geology*, 56, 27-40.

Richardson, E. V., D. B. Simons, and G. J. Posakony (1961), Sonic depth sounder for laboratory and field use, *U.S. Geol. Survey Circular*, 450, 1-7.

Schindler, R. J., D. R. Parsons, L. Ye, J. A. Hope, J. H. Baas, J. Peakall, A. J. Manning, R. J. Aspden, J. Malarkey, S. Simmons, D. M. Paterson, I. D. Lichtman, A. G. Davies, P. D. Thorne, and S. J. Bass (2015), Sticky stuff: Redefining bedform prediction in modern and ancient environments, *Geology*, 43 (5), 399-402.

Shepard, F. P. (1954), Nomenclature based on sand-silt-clay ratios, *Journal of Sedimentary Petrology*, 24, 151-158.

Shields, A. (1936), Anwendung der Ähnlichkeitsmechanik und der Turbulenzforschung auf die Geschiebebewegung, *Mitteilungen der Preussischen Versuchsanstalt für Wasserbau und Schiffbau*, 26, 1-26.

Shimeta, J and P. A. Jumars (1991), Physical mechanisms and rates of particle capture by suspension feeders, *Oceanog. Mar. Biol. Ann. Rev.*, 29, 191–257.

Shvidchenko, A. B., G. Pender and T. B. Hoey (2001), Critical shear stress for incipient motion of sand/gravel streambeds, *Water Resources Research*, 37, 2273-2283.

Simons, D. B., E. V. Richardson, and C. F. Nordin (1965), *Bedload equation for ripples and dunes, Professional paper 462-H, USGS*, United States Government Printing Office, Washington.

Smyth, C. E., and M. Z. Li (2005), Wave-current bedform scales, orientation, and migration on Sable Island Bank, *Journal of Geophysical Research*, 110, C02023.

Soulsby, R. (1997), *Dynamics of Marine Sands: A Manual for Practical Applications*, Thomas Telford, London.

Soulsby, R. (2006), *Simplified Calculation of Wave Orbital Velocities, Report TR 155*, HR Wallingford, Wallingford, UK.

Soulsby, R. L., and S. Clarke (2005), *Bed Shear-stresses Under Combined Waves and Currents on Smooth and Rough Beds, Report TR 137*, HR Wallingford, Wallingford, UK.

Soulsby, R. L., L. Hamm, G. Klopman, D. Myrhaug, R. R. Simons, and G. P. Thomas (1993), Wave-current interaction within and outside the bottom boundary layer, *Coastal Engineering*, 21, 41-69.

Soulsby, R. L., R. J. S. Whitehouse, and K. V. Marten (2012), Prediction of time-evolving sand ripples in shelf seas. *Continental Shelf Research*, 38, 47-62.

Souza, A. J., P. S. Bell, and L. Amoudry (2010), Working toward a common strategy for U.K. sediment transport research. *EOS, Transactions American Geophysical Union*, 91 (5), 45-46.

Souza, A. J., and A. Lane (2013), Effects of freshwater inflow on sediment transport, *Journal of Operational Oceanography*, 6 (1), 27-31.

Spearman, J. R., A. J. Manning, and R. J. S. Whitehouse (2011), The settling dynamics of flocculating mud and sand mixtures: Part 2 – Numerical modelling, *Ocean Dynamics*, 61(2), 351-370, doi: 10.1007/s10236-011-0385-8.

Sternberg, R. W. (1967), Measurements of sediment movement and ripple migration in a shallow marine environment, *Marine Geology*, 5, 195-205.

Sutton, M. A., J.-J. Orteu, and H. Schreier (2009), *Image Correlation for Shape, Motion and Deformation Measurements: Basic Concepts, Theory and Applications*, Springer Science, New York.

Thorne, P. D., and Hanes, D. M. (2002), A review of acoustic measurement of small-scale sediment processes. *Continental Shelf Research*, 22, 603-632.

Tolhurst, T. J., A. J. Underwood, R. G. Perkins, and M. G. Chapman (2005), Content versus concentration: Effects of units on measuring the biogeochemical properties of soft sediments, *Estuarine, Coastal and Shelf Science*, 63, 665-673.

Tolhurst, T. J., K. S. Black, and D. M. Paterson (2009), Muddy Sediment Erosion: Insights From Field Studies, *Journal of Hydraulic Engineering*, 135 (2), 73-87.

Underwood, G., D. M. Paterson, and R. Parkes (1995), The measurement of microbial carbohydrate exopolymers from intertidal sediments, *Limnology and Oceanography*, 40, 1243–1253.

van de Koppel, J., P. M. J. Herman, P. Thoolen, and C. H. R. Heip (2001), Do alternate stable states occur in natural ecosystems?, *Ecology*, 82 (12), 3449-3461.

van den Berg, J. H. (1987), Bedform migration and bed-load transport in some rivers and tidal environments, *Sedimentology*, 34, 681-698.

van den Berg, J. H., and A. van Gelder (1993), A new bedform stability diagram, with emphasis on the transition of ripples to plane bed in flows over fine sand and silt, in *Alluvial Sedimentation*, (International Association of Sedimentologists Special Publication 17), edited by M. Marzo and C. Puigdefábregas, pp. 11–21, Blackwell Publishing Ltd., Oxford, UK.

van der Mark, C. F., A. Blom, and S. J. M. H. Hulscher (2008), Quantification of variability in bedform geometry, *Journal of Geophysical Research*, 113, F03020, doi: 10.1029/2007JF000940.

van Ledden, M., W. G. M van Kesteren, and J. C. Winterwerp (2004), A conceptual framework for the erosion behaviour of sand-mud mixtures. *Continental Shelf Research*, 24, 1-11.

van Rijn, L. C. (1984), Sediment transport, part III: bed forms and alluvial roughness, *Journal of Hydraulic Engineering*, 110 (12), 1733-1754.

van Rijn, L. C. (2006), Bed form tracking, *Manual Sediment Transport Measurements in Rivers Estuaries and Coastal Seas*, Sub-section 5.5.2., Delft Hydraulics Laboratory, Delft, The Netherlands.

Villaret, C., N. Huybrechts, A. G. Davies, and O. Way (2011), Effect of bed roughness prediction on morphodynamic modelling: application to the Dee estuary (UK) and to the Gironde estuary (France). In *Proceedings of 34th IAHR World Congress*, 1149–1156.

Waeles, B., P. Le Hir, and P. Lesueur (2008), A 3D morphodynamic process-based modelling of a mixed sand/mud coastal environment: the Seine estuary, France, *Proceedings in Marine Science, Volume 9, Sediment and Ecohydraulics: INTERCOH*, 477-498.

Wentworth, C. K. (1922), A scale of grade and class terms for clastic sediments, *The Journal of Geology*, 30 (5), 377-392.

Whitehouse, R., R., Soulsby, W., Roberts, and H., Mitchener, (2000), *Dynamics of estuarine muds: A manual for practical applications*. London: Thomas Telford.

Wiberg, P. L., and C. R. Sherwood (2008), Calculating wave-generated bottom orbital velocities from surface-wave parameters, *Computers & Geosciences*, 34, 1243-1262.

Wilcox, R. R., (2012), *Introduction to Robust Estimation and Hypothesis Testing*, 3rd Ed., Elsevier, Waltham, MA.

Winterwerp, J. C., and W. G. M. van Kesteren (2004), *Introduction to the Physics of Cohesive Sediment in the Marine Environment*. Developments in sedimentology 56. Elsevier B. V., Amsterdam.

Wotton, R. S. (2004), The essential role of exopolymers (EPS) in aquatic systems. In *Oceanography and Marine Biology*: *An Annual Review*, 42, CRC, 57-64.

Yalin, M. S. (1977), *Mechanics of Sediment Transport*, 2nd ed., Pergamon Press, Oxford.

Appendix A: list of notation

c	Bed clay content (vol%)
e	Bed EPS content (wt%)
f	Bedform shape factor (-)
h	Water depth/height above bed (m)
n	Number of measurements or values (-)
p	Probability extreme value occurrence (-)
q_b	Volume bed material transport rate ($m^3\ m^{-1}\ s^{-1}$)
s	Relative density of sediment to water (-)
$\langle u \rangle$	Depth mean current velocity ($m\ s^{-1}$)

u_b	Bedform migration rate (m s^{-1})
u_w	Bottom wave orbital amplitude velocity (m s^{-1})
z_0	Bed roughness length (m)
B	Bandwidth of migration rate (m^{-1})
C	95% correlation confidence interval (m)
D_{50}	Median grain diameter (m)
D_*	Dimensionless grain diameter
E_{nrms}	Normalized RMS correlation error (-)
H_{s}	Significant wave height (m)
K	Hubbell's loss-gain factor (-)
P	Bed porosity (-)
Q_b	Mass bed material transport rate (kg m^{-1} s^{-1})
R^2	Correlation coefficient (-)
R_{nn}	Correlation function (-)
T_p	Peak wave period (s)
T_{rl}	Record length of cross-correlation (m)
α	Coefficient in equation 2 (m s^{-1})
β	Coefficient in equation 2
η, η_{eq}	Bedform height, ripple equilibrium height (m)
θ, θ'	Total Shields parameter, skin friction Shields parameter (-)
λ, λ_{eq}	Bedform length, ripple equilibrium length (m)
v	Kinematic viscosity of water (m^2 s^{-1})
ρ, ρ_{s}	Water density, sediment density (kg m^{-3})
$\rho_{12}(\tau^*)$	Peak normalized cross-correlation (-)
$\sigma(\tau^*)$	Standard deviation of the peak cross-correlation (m)

τ'_c, τ'_w, $\tau'_{\max}$, $\tau'_{\max l}$	Current-only bed shear stress, wave-only bed shear stress, combined maximum bed shear stress, linear maximum bed shear stress (skin friction only) (N m^{-2})
τ^*	Peak correlation lag (m)
φ	Angle between wave and current direction (degrees)

Appendix B: Malarkey and Davies's (2012) model

The Malarkey and Davies (2012) model, which is a modification of the Soulsby and Clarke (2005) model, requires the following input quantities:

$$\boldsymbol{h},\quad \boldsymbol{z_0},\quad \boldsymbol{u_w},\ \boldsymbol{T_p},\quad \langle \boldsymbol{u} \rangle,\quad \boldsymbol{\varphi}. \tag{B1}$$

These inputs allow the calculation of the equivalent current-alone and wave-alone stresses, τ_c and τ_w, respectively. Here, $\tau_c = \rho C_D \langle u \rangle^2$ and $\tau_w = ½\rho f_w u_w^2$, where $C_D = \kappa^2/\log^2(h/z_0\mathrm{e})$ is the drag coefficient, $\kappa = 0.4$ is the von Kármán constant, $f_w = 1.39(a_w/z_0)^{-0.52}$ is the friction factor, $a_w = u_w/\omega$ is the wave orbital amplitude and $\omega = 2\pi/T_p$. If the process is completely linear, the maximum stress, $\tau_{\max l}$, is given by:

$$\boldsymbol{\tau_{\mathrm{max}l}} = \sqrt{\boldsymbol{\tau_c^2 + \tau_w^2 + 2\tau_c\tau_w|\cos\varphi|}}\,. \tag{B2}$$

However, in the case of Malarkey and Davies' (2012) stronger non-linear option, the combined maximum stress in the wave cycle, $\tau_{\max}$, is given by:

$$\boldsymbol{\tau_{\mathrm{max}}} = \sqrt{\boldsymbol{\tau_m^2(1+\varepsilon_1+\varepsilon_2) + \tau_p^2 + 2\tau_m\tau_p\sqrt{1+\varepsilon_1+\varepsilon_2}|\cos\varphi|}}\,, \tag{B3}$$

where τ_m is the combined-mean stress, τ_p is the combined-wave stress and ε_1 and ε_2 are additional scaling terms that were introduced to make the maximum stress more consistent with numerical model results. Since τ_m, τ_p, ε_1 and ε_2 are all determined in terms of the input conditions (see Malarkey and Davies, 2012), $\tau_{\max}$ can also be determined in terms of the input conditions.

Appendix C

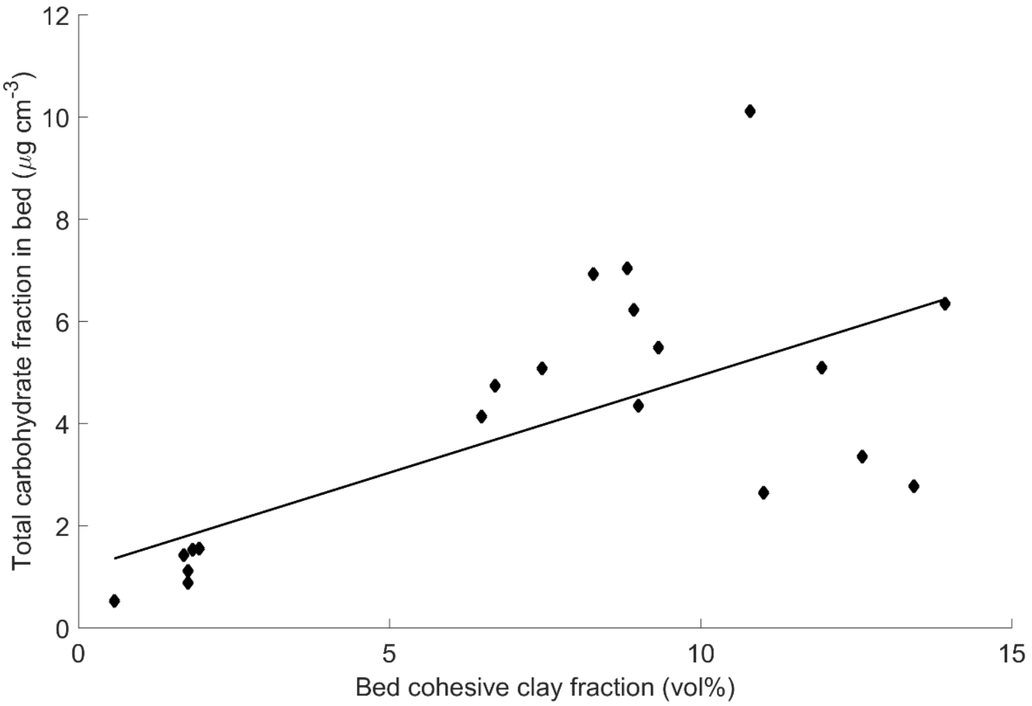

Figure C1: Total carbohydrate fraction by volume against bed cohesive clay fraction, derived from bed samples collected in the vicinity of Sites 1 to 3 (analyzed for EPS and particle size). The black line represents a robust linear regression fit ($R^2 = 0.42$, $p < 0.05$, for $n = 20$, total carbohydrate fraction by volume $= 0.38c + 1.13$) between the cohesive clay and total carbohydrate values.